Sci. Dril., 35, 127–157, 2026
https://doi.org/10.5194/sd-35-127-2026

Scientific Drilling
Open Access

Initial results from a Trans-Amazon Drilling Project core from the Acre Basin of Brazil

Sherilyn C. Fritz[1], André O. Sawakuchi[2], Anders Noren[3], Paul A. Baker[4], Cleverson Silva[5], Carlos Jaramillo[6], Renato Paes de Almeida[2], Liliane Janikian[7], Isaac Salém Bezerra[2], Marcos Barbosa[8], Dailson Bertassoli[2], Rain Blankenship[9], Cristiano M. Chiessi[10], Sarah J. Feakins[9], Maria da Glória Garcia[2], Cécile Gautheron[11], Brian Grivna[3], Gelvam Hartmann[12], Cindy Kunkel[13], André Marconato[2], Angela Martinez[2], Sebastian G. Marulanda[2], Carlos Eduardo M. Mazoca[2], Francisco R. Negri[14], Mauricio Parra[2], Werner E. Piller[15], Fabiano N. Pupim[2], Victor Salgado[5], Rachel T. So[9], Priscila Emerich Souza[2], Elena Stiles[16], Caroline A. E. Strömberg[16], Siu Mui Tsai[17], Ingo Wahnfried[18], Josh West[9], Marc-Élie Adaimé[19], Jhon Afonso[12], Thomas Kenji Akabane[2], Camila Eliza Althaus[2], Carlos D'Apolito[20], Kleiton R. Araújo[2], Roney da Silva de Azevedo Júnior[18], Jessica Barcellos[5], Tacio Bicudo[2], Giovanni Bogota[21], Bodo Bookhagen[22], Caio Breda[2], Alderlene Pimentel de Brito[18], Francy Carvajal[23], Daniel Antunes Coppi[12], Carolina Barbosa Leite da Cruz[2], Felipe Torres Figueiredo[24], Kate Freeman[25], Pedro Victor Oliveira Gomes[2], Martin Gross[26], Emma Hartke[25], Katja Heeschen[13], William Mozart Henrichs[2], Leonardo Henrique[2], Carina Hoorn[27], Brian K. Horton[28], Andrés Díaz-Jamamillo[6], Said Kamrani-Mehni[13], Fatima Leite[6], Lin Li[29], Rodrigo Ferreira de Lucena[2], Alastair Milne[30], Thomás Miranda[2], Marcelo Mota[2], Diana Ochoa[31], Vinicius de Lima Passos[2], Rafaela Maciel Lopes de Paula[2], Elisa Piispa[32], Angelo Plata Torres[6,33], Surangi W. Punyasena[19], Adriano Domingos dos Reis[34], Catherine Rigsby[35], Andrés F. Salazar Rios[15], Fernanda Costa Gonçalves Rodrigues[2], Raquel M. M. Romão[2], Ingrid C. Romero[6,36], Henrique O. Sawakuchi[37], Doug Schnurrenberger[3], Kristina Brady Shannon[3], Silane A. F. da Silva-Caminha[6,38], Clauses Sousa[2], Larissa Natsumi Tamura[2], Thomas Wiersberg[13], Helanlin Xiang[27], and Belén Zamudio[15]

[1]Department of Earth and Atmospheric Sciences and School of Biological Sciences, University of Nebraska-Lincoln, Lincoln, NE, USA
[2]Institute of Geosciences, Universidade de São Paulo, São Paulo, Brazil
[3]Continental Scientific Drilling (CSD) Facility, University of Minnesota, Minneapolis, MN, USA
[4]Division of Earth and Climate Sciences, Duke University, Durham, NC, USA
[5]Department of Geology, Universidade Federal Fluminense, Niteroi, Brazil
[6]Center for Tropical Paleoecology and Archeology, Smithsonian Tropical Research Institute, Panama City, Panama
[7]Department of Ocean Sciences, Federal University of São Paulo, São Paulo, Brazil
[8]Acqua Terra, São Paulo, Brazil
[9]Department of Earth Sciences, University of Southern California, Los Angeles, CA, USA
[10]School of Arts, Sciences, and Humanities, Universidade de São Paulo, São Paulo, Brazil
[11]Institute of Earth Sciences, Université Grenoble Alpes, Université Savoie Mont Blanc, CNRS, IRD, IFSTTAR, Grenoble, France
[12]Institute of Geosciences, Universidade Estadual de Campinas, Campinas, Brazil
[13]GFZ Helmholtz Centre for Geosciences, Potsdam, Germany
[14]Laboratory of Paleontology, Universidade Federal do Acre, Cruzeiro do Sul, Brazil
[15]Institute for Earth Sciences, Universität Graz, Graz, Austria
[16]Department of Biology and Burke Museum, University of Washington, Seattle, WA, USA
[17]Center for Nuclear Energy in Agriculture, Universidade de São Paulo, São Paulo, Brazil

Published by Copernicus Publications on behalf of the IODP and the ICDP.

[18]Geosciences Department, Universidade Federal do Amazonas, Manaus, Brazil
[19]Department of Plant Biology, University of Illinois – Urbana-Champaign, Urbana, IL, USA
[20]Faculty of Biological and Environmental Sciences, Universidade Federal da Grande Dourados, Dourados, Brazil
[21]Faculty of Environment and Natural Resources, Universidad Distrital Francisco José de Caldas, Bogotá, Colombia
[22]Institute of Geosciences, Universität Potsdam, Potsdam, Germany
[23]Ensenada Center for Scientific Research and Higher Education, Ensenada, Mexico
[24]Department of Geology, Federal University of Sergipe, São Cristóvão, Brazil
[25]Department of Geosciences, Pennsylvania State University, University Park, PA, USA
[26]Department of Geology and Paleontology, Universalmuseum Joanneum, Graz, Austria
[27]Institute for Biodiversity and Ecosystem Dynamics, Universiteit van Amsterdam, Amsterdam, the Netherlands
[28]Department of Earth and Planetary Sciences, University of Texas at Austin, Austin, TX, USA
[29]Department of Earth, Environmental, and Geographic Sciences, University of North Carolina – Charlotte, Charlotte, NC, USA
[30]Edinburgh Geological Society, Edinburgh, Scotland, UK
[31]Department of Geology, Universidad de Salamanca, Salamanca, Spain
[32]Institute of Earth Sciences, University of Iceland, Reykjavik, Iceland
[33]Department of Geological Sciences, Universidad de Caldas, Manizales, Colombia
[34]Institute of Geosciences, University of Brasilia, Brasilia, Brazil
[35]Department of Geological Sciences, East Carolina University, Greenville, NC, USA
[36]Smithsonian National Museum of Natural History, Washington, D.C., USA
[37]Department of Thematic Studies, Linköping University, Linköping, Sweden
[38]Faculty of Geosciences, Universidade Federal de Mato Grosso, Cuiabá, Brazil

Correspondence: Sherilyn C. Fritz (sfritz2@nebraska.edu)

Received: 15 October 2025 – Revised: 10 April 2026 – Accepted: 17 May 2026 – Published: 26 June 2026

Abstract. The Trans-Amazon Drilling Project (TADP) is reconstructing the late Cenozoic history of Amazonian geology, climate, rivers, and forests. Drilling in the Acre Basin of western Brazil in 2023 recovered an 860 m drill core characterized by sediments that were deposited in a large paleo-river system. The overall sequence includes sandstones, siltstones, and mudstones that underwent varied degrees of weathering and pedogenesis. Here, we describe the ongoing geochronologic, geochemical, mineralogical, geophysical, and biotic analyses of the sedimentary record and present some preliminary inferences of the environmental history based on these initial results.

Except for the uppermost ∼12 m, sediments from the drill core represent a single lithostratigraphic unit, assigned to the Solimões Formation, which is dominated by feldspar-rich sands of Andean origin. The pollen assemblage is quite different from Early to Middle Miocene floras that have been analyzed from a few sites elsewhere in the western Amazon. The novel pollen assemblage and new geochronological results suggest that the sequence may span the latest Miocene and all of the Pliocene Epoch, an interval that currently is not well represented in existing regional records and that is crucial for understanding the evolution of Amazonian biodiversity, as well as landscape transformations driven by Andean uplift and global climate change.

1 Introduction

1.1 Trans-Amazon Drilling Project (TADP) objectives and project overview

The Amazon and Andean montane forest biomes host Earth's highest biodiversity, which evolved in a complex landscape formed by dynamic geologic and climatic processes across space and through time. Despite extensive study, many questions remain about the pattern of biodiversity change through time and the role of the changing physical landscape in affecting that evolutionary trajectory (Baker et al., 2015).

Most existing studies of the assembly and diversity of the Amazon forest consist of isolated snapshots in space and time, primarily from outcrop studies or drill core samples retrieved for coal or petroleum exploration (Kern et al., 2020;

Hoorn et al., 2023; Jaramillo et al., 2025). As a result, it is unclear whether biotic diversification proceeded at a constant rate or episodically. Likewise, major aspects of the evolution of the physical landscape remain unknown, including (1) the spatio-temporal variability of temperature and precipitation (e.g., Cheng et al., 2013), (2) the temporal development of the Amazon fluvial system and its subbasin connectivity (e.g., Bicudo et al., 2019; Almeida et al., 2024), and (3) the nature and extent of major wetland or lacustrine systems in the western Amazon (e.g., Gross and Piller, 2020; Hoorn et al., 2022).

The Amazon Basin is vast, extending more than 3000 km from the distal Andean foreland basins to the mouth of the Amazon River, and it is characterized by large variability in vegetation, climate, and fluvial morphology. The Brazilian Amazon is underlain by continental basement rocks exposed in the Guyana and Central Brazil plateaus, and has a Mesozoic-Cenozoic fluvial sediment cover. It is composed of four Paleozoic sedimentary basins (Acre, Solimões, Amazonas, and Marajó), which are separated by structural highs (the Iquitos, Purus, and Gurupá arches) (Fig. 1). The structural highs may have served as topographic barriers at various times since the Paleozoic, possibly affecting the Cenozoic evolution of the Amazon fluvial network (Figueiredo et al., 2009; Caputo and Soares, 2016) and its biota (Ribas et al., 2012).

The aim of the Trans-Amazon Drilling Project was to recover long continuous drill cores spanning the Cenozoic to reconstruct the evolutionary history of the climate, river system, and forests of the Amazon using state-of-the-art geochronologic, geochemical, mineralogical, geophysical, and biotic analyses of the sedimentary record. The project is also investigating the aquifers, subsurface microbial life, and light hydrocarbons derived from burial alteration of organic sediments. Sedimentary basins hosting petroleum and natural gas accumulations are important sources of methane to the atmosphere (Etiope and Schwietzke, 2019), and the Amazon hosts extensive hydrocarbon-bearing basins.

The TADP was developed under the auspices of the International Continental Scientific Drilling Program (ICDP), and its original plan was to drill a west to east transect of sites in each of the major continental sedimentary basins in Brazilian territory and in the offshore Foz do Amazonas Basin (Baker et al., 2015). Based on funding constraints for large drilling projects, the scope was reduced to three continental sites, one each in the Acre, Amazonas, and Marajó basins. Ultimately, because of cost increases following the COVID-19 pandemic, TADP drilled one site in the western basin of Acre (TADP-1A) and one site in the eastern Marajó Basin (TADP-2A) (Table 1). The history of the central Amazonas Basin is being investigated from an industry drill core (PBAT-15-43) that was donated to TADP by Brazil Potash (Fig. 1). The planned offshore drilling (originally scheduled as International Ocean Discovery Program (IODP) Expedition 387) was postponed when the required permissions were not issued and ultimately could not be rescheduled due to the retirement of the *JOIDES Resolution*. This paper presents an overview of preliminary observations of the long drill core recovered from the Acre Basin, including initial results on the age and landscape history of the western Brazilian Amazon, along with data on pore-water chemistry, methane production, and the geomicrobiology of its buried sediments.

1.2 Acre specific objectives

The Acre Basin of the western Amazon (Fig. 2) is a distal Andean foreland basin and is well situated to record the influences of Andean tectonism, erosion, and climate on the evolution of western Amazon biota. The basin is sufficiently close to the Andes to have received sand and silt with Andean provenance containing detrital zircon grains and other minerals suitable for dating and provenance analyses. Yet, it is sufficiently distal from the Andes to have accumulated a thick sequence of finer-grained sediment, often amenable to the preservation of pollen and other microfossils. Today, the western Amazon is significantly wetter than areas to the east, and the dry season is considerably shorter in the west than the east. More than 2000 mm of precipitation falls annually in the Acre Basin today (Espinoza et al., 2009), the majority of which occurs during the austral summer (DJF) when the near-continental-scale South American monsoon is most intense. Tree alpha diversity is also higher today in the western Amazon than in the eastern Amazon (ter Steege, 2013). Whether (and when) similar precipitation and diversity gradients existed in the past are major questions for the TADP.

The nature of Neogene depositional environments in the western Amazon is controversial (Jaramillo et al., 2017). Different authors have variously proposed ancient depositional systems that were interpreted as long-lived or short-lived (on the order of 1 million years or less) marine transgressions, marine embayments, or tidal wetlands (Webb, 1995; Espurt et al., 2007; Räsänen et al., 1995); long-lived mega-lakes (Frailey et al., 1988); long-lived mega-wetlands (Wesselingh et al., 2006); or fluvial-dominated environments akin to the present-day large rivers and floodplain lakes (Latrubesse et al., 2007; Gross et al., 2013). The Acre drill site is well situated for characterizing sedimentary environments over a large region of the western Amazon, as well as hydrological and landscape changes during the Neogene, which is the period when much of the extant biodiversity originated (Rull, 2011).

2 Geology of the Acre Basin

The Acre Basin is part of the Andean foreland basin system (Horton, 2018; Oliveira and Vidotti, 2024) and shares some tectonic history with the Marañón, Ucayali, and Madre de Dios basins to the west and south (Cunha, 2007). The infill of the basin is predominantly composed of sandstone and shale, with minor carbonate sequences, including a pre-orogenic

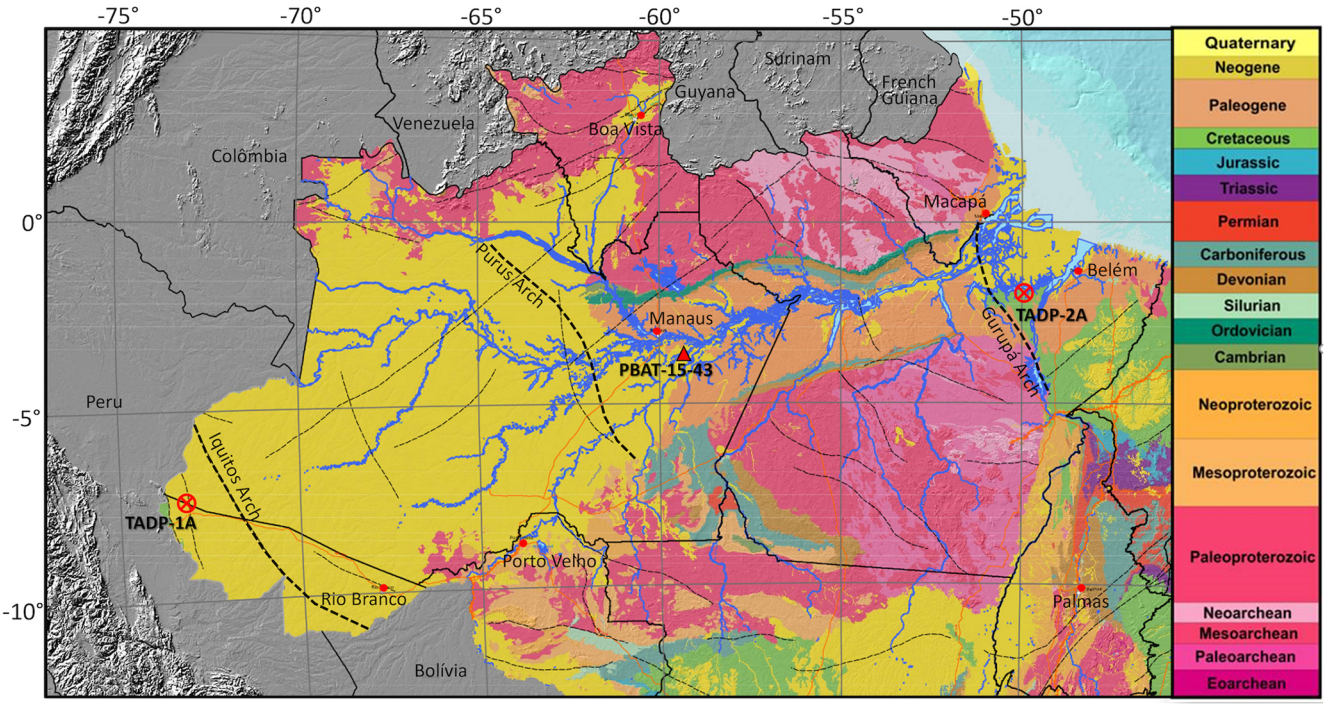

Figure 1. Geologic map of the Amazon (CPRM, 2015) showing the locations of the two completed continental ICDP drill sites in the Acre (TADP-1A) and Marajó (TADP-2A) basins, as well as a core in the Amazonas Basin (PBAT-15-43) that was donated to the TADP by Brazil Potash.

Paleozoic sequence and syn-orogenic sequences from the Mesozoic and Cenozoic eras. The maximum recorded thicknesses of these sequences are respectively 1500, 4000, and 2200 m (Cunha, 2007). Importantly, the Andean zone to the west of the Acre Basin, between 2 and 15° S, is today a region of flat-slab subduction with no active arc volcanism occurring along its length (Bishop et al., 2017).

Stratigraphic sequences from the Solimões Basin to the northeast of the Acre Basin can be correlated with specific stratigraphic levels of the Acre Basin (Wanderley-Filho et al., 2010), while dynamic topography can account for stratigraphic offset between basins of the syn-orogenic successions (Bicudo et al., 2020; Sacek et al., 2023). The forebulge area that separates the Acre and Solimões basins – the Iquitos Arch (Fig. 1) – is characterized by a thinner Cenozoic sedimentary sequence than in the basin depocenters on either side (Maia et al., 1977).

The Miocene to Pliocene Subandean sedimentary basin recorded shortening followed by an uplift event, possibly of late Pliocene age (Espurt et al., 2007; Gautheron et al., 2013), which inverted the Acre Basin and is responsible for the current elevation of more than 600 m above sea level in the area known as the Fitzcarrald Arch (Fig. 2). Despite this uplift, surface exposures in the Acre Basin are primarily limited to Cenozoic strata, predominantly Late Miocene fossil-bearing successions (Negri et al., 2010). These are mapped as part of the Solimões Formation (Cunha, 2007), with its type section located in the Solimões Basin. In the westernmost part of the Acre Basin, a reverse fault system of Cenozoic age accounts for local exposures of Cretaceous successions in the Divisor Range (Wanderley-Filho et al., 2010).

Local basement consists of magmatic and metamorphic rocks from the southwestern margin of the Amazon Craton, specifically the 1.5 to 1.3 Ga Rondoniano-San Ignácio orogenic belt (Tassinari et al., 1996, 2000). However, previous studies indicate Andean-dominated provenance for sediments of the Solimões Formation in the Acre Basin (Roddaz et al., 2005; Horbe et al., 2019).

3 Methods

3.1 Field

3.1.1 Mobilization and drilling

The Acre drill site (7°43′30.09″ S, 72°38′57.44″ W) is located near oil exploration well 2-CDST-1-AC (Agência Nacional do Petróleo, Gás Natural e Biocombustíveis – ANP) in the Municipality of Rodrigues Alves (AC) (Fig. 3). The drill site is situated on private land on a terrace of the western bank of the Juruá River (Fig. 4), adjacent to the urban area of Rodrigues Alves and with road access through the BR-364 highway. Drilling equipment was mobilized from Mariana (MG) in southeastern Brazil, ∼ 4400 km to the east, and arrived in Rodrigues Alves on 29 May 2023. Drilling com-

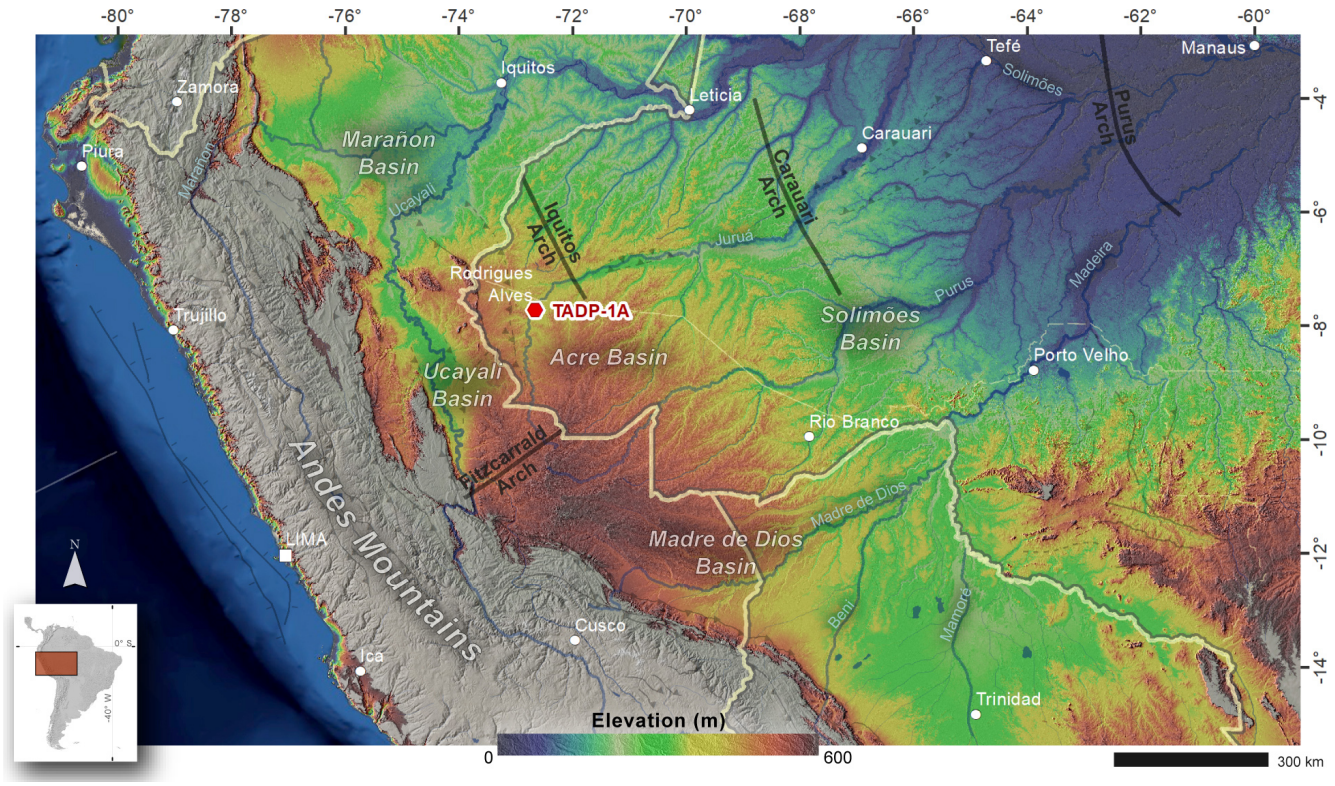

Figure 2. Location map of the TADP-1A drill site in the Acre Basin, southwestern Amazonia. The hypsometric background is derived from the NASA digital elevation model (DEM) (NASA JPL, 2021), a reprocessed version of the SRTM dataset, originally at 1 arcsec (∼ 30 m) resolution and here resampled to ∼ 250 m. Elevation values are constrained between 0 and 600 m to emphasize lowland geomorphic features, with color-shaded relief overlain on a hillshade generated from the same DEM. NASADEM vertical and horizontal accuracies typically range from ∼ 3–10 and ∼ 10–20 m, respectively, depending on terrain. Vector layers (political boundaries, rivers, structural arcs and features, and localities) are sourced from the Tectonic Map of South America (Cordani et al., 2016), and all GIS processing was conducted using QGIS and ArcGIS.

Table 1. Overview of TADP holes.

Hole name	ICDP name	IGSN	Coordinates (latitude, longitude)
TADP-1A	5066_1_A	ICDP5066E01AH50001	−7.7265, −72.64622
TADP-2A	5066_2_A	ICDP5066E02AH60001	−1.8819, −50.21876

menced on 16 June 2023, and on-site operations ended on 22 December 2023, with well abandonment. During most of this time, there was a full retinue of drillers (∼ 30 persons) and scientists (∼ 6–8 persons) on site.

Slimhole drilling was undertaken by GEOSOL SA using a Boart Longyear LF230 wireline diamond coring rig, 275HP, rated for 22.8 t maximum pull, with a chuck drive and 9 m rod pull. The first phase of drilling reached 40 m depth with PQ coring tools (core diameter of 8.3 cm), followed by borehole enlargement to 12.25 in. (31.1 cm) for 10 in. (25.4 cm) casing installation. PQ coring continued to a depth of 550 m, followed by borehole enlargement to 8.5 in. (21.6 cm) for 5.75 in. (14.6 cm) casing installation. PQ coring again continued to 746 m, followed by a reduction in diameter, with the final phase cored with HQ coring tools (6.3 cm) to the basal depth of 923 m.

Before and during drilling, outreach activities were performed to inform the local communities about the purposes of the drilling and to disseminate scientific information related to the goals of the TADP (see Sect. 5 for more details).

3.1.2 Field sampling

After each drilling run, the cores were delivered to the scientific team, which operated in two 12 h shifts (day and night). The cores were cut into sections of up to 150 cm, following standard protocols to accommodate core handling, scanning instrumentation, and archiving.

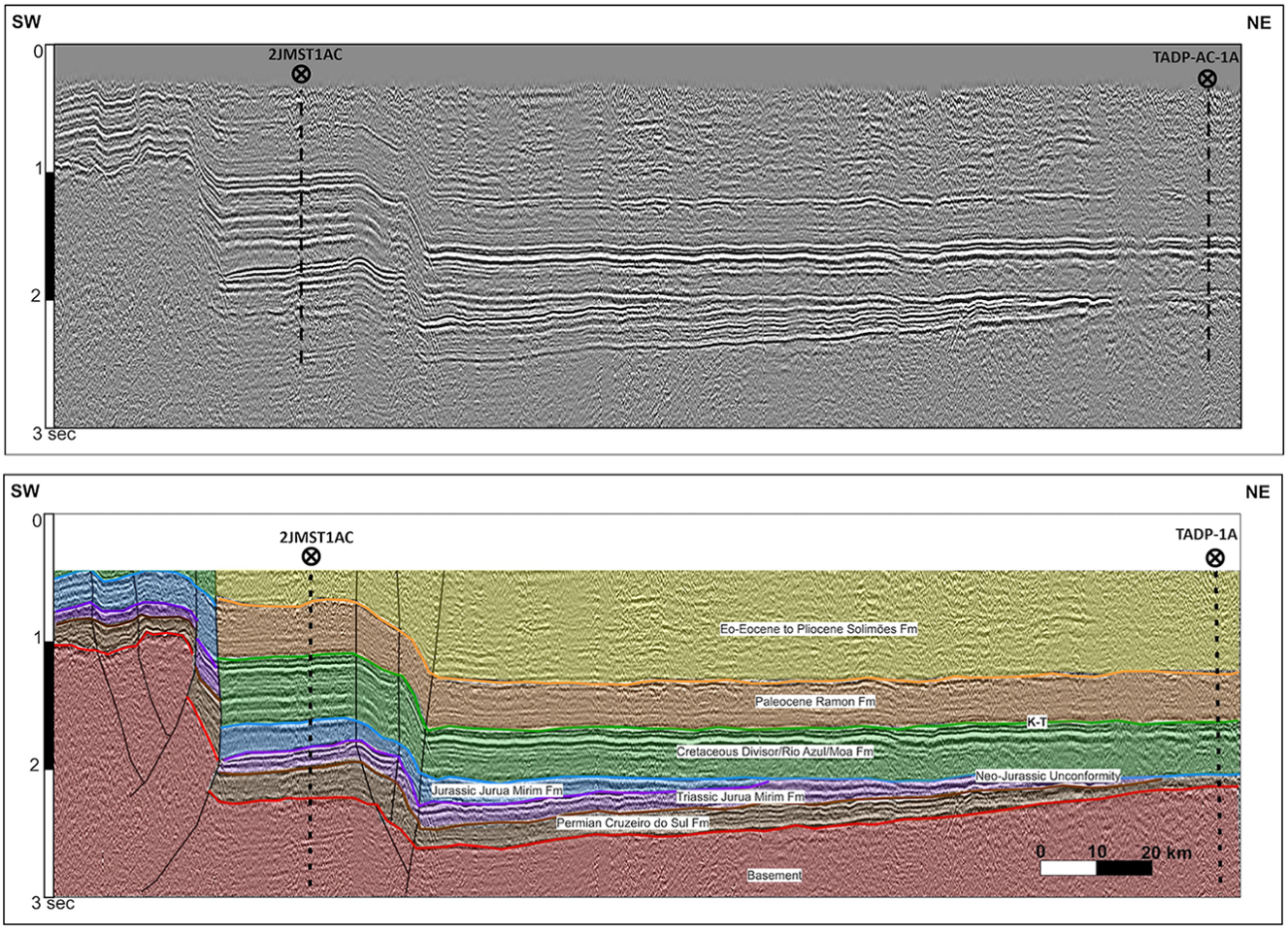

Figure 3. Seismic line (upper) and interpreted seismic line (lower) for the Acre Basin drilling site. The TADP-1A drill site is at the same location as industry well 2CDST1AC and to the right of well 2JMST1AC. Colors correspond to the geologic map in Fig. 1.

Each section was labeled, then sealed with end caps at both ends, using blue tape on the top cap and red tape on the bottom cap to indicate core orientation. The sections were cut using a handsaw for soft cores and a wet saw for more consolidated cores. Each section was then weighed and measured. During drilling, the scientific team performed basic sedimentological descriptions using core catcher samples and sampled for geomicrobiology, pore gases, and pore waters.

All on-site core and section data, as well as the lithological description and all on-site samples, were recorded in ICDP's mobile Drilling Information System (mDIS), and labels for the samples were printed directly out of the system. Furthermore, to follow FAIR principles (Wilkinson et al., 2016), mDIS automatically assigns a globally unique identifier – the International Generic Sample Number (IGSN) – to holes, cores, sections, and samples.

Sedimentological descriptions and core catcher sampling. A 5–10 g sample was taken from each core catcher and stored in a labeled plastic bag. A small fraction (~ 1 g) was used for a preliminary sedimentological description (texture and composition) under a binocular microscope, applying the Folk classification system and using hydrochloric acid (10 %) to identify the presence of carbonate minerals. The remaining sample was stored and sent to the Institute of Geosciences at the University of São Paulo for preliminary luminescence analyses to characterize sand maturity and provenance.

Geomicrobiology sampling. A sample was collected every 20 m down to 200 m depth and approximately every 100 m below that, using a 1–3 cm core segment taken immediately after core retrieval. The surface of each sample was scraped with a sterile spatula to remove potential contaminants. For molecular analysis, ~ 20 g of sediment was collected with a sterile spatula and preserved in LifeGuard Soil Preservation Solution. Subsamples were stored in 20 or 50 mL Falcon tubes at 20 or 4 °C until processing and were transported under ice to the laboratory in São Paulo.

Pore gas sampling. Pore gas was collected using a headspace approach. Samples were collected every 20 m down to 200 m depth and every 50 m below that, using a 1–

Figure 4. Drilling rig at the site of the TADP-1A well in the Acre Basin, Municipality of Rodrigues Alves (AC). Photograph by Isaac Bezerra.

5 cm whole round (WR) core slice immediately after core retrieval and above the segment used for pore-water sampling (see below). Each sample was placed in a labeled gas-tight bag, sealed with a manual heat sealer, and stored in a vacuum chamber for 30 min, followed by extraction of 5 cm^3 (5 mL) of gas for analysis.

Pore-water sampling. Fifteen WR samples were taken approximately every 20 m, from 20 to 220 m depth, and then approximately every 100 m until 630 m depth, with core lengths ranging from 20 to 50 cm. The surface of each WR was scraped with a spatula to remove potential contamination from drilling fluids and sediment smearing in the borehole. The remaining sediment was placed into the pore-water extractor fitted with Whatman Number 1 filters. The assembly was placed in a manual hydraulic press, and gauge forces of up to 15 t were applied. Water was extruded into a clean plastic syringe and then dispensed from the syringe through a 0.2 µm sterilized polysulfone disposable filter into labeled 2 mL brown glass vials. Drilling mud samples were also collected from the mud-shaker as a reference for potential contamination, because groundwater extracted from local wells was used to make the drilling mud. Water samples were also collected from the Juruá River, local springs, shallow piezometers, and water wells of up to 80 m depth for comparison. Samples were shipped to USP in São Paulo for $\delta^{18}O$ and $\delta^{2}H$ analyses on a laser absorption spectrometer, model L2130-i, from Picarro.

3.1.3 Geophysical downhole logging

Borehole logging was conducted in both cased and open-hole sections. After coring to 558 m depth, open hole logs were conducted to provide a stratigraphic framework for interpreting online gas analysis and core analyses, and to evaluate operational issues such as borehole conditions. The logging was executed using a slimhole wireline system (Mount Sopris Instruments), equipped with caliper, natural gamma, magnetic susceptibility, resistivity, sonic, and fluid temperature and conductivity probes. Magnetic susceptibility and resistivity were only acquired from 40 to 558 m depth due to the 10 in. (254 mm) conductor casing installed from 0 to 40 m. Drilling operational constraints (stuck pipe to 751 m, borehole collapse below this level; see the TADP Operational Report Sect. 4.1 for details) prevented open hole downhole logging below 558 m depth.

After installing 5.75 in. (146.05 mm) casing from 0 to 558 m, the full waveform sonic (FWS) tool was run to perform a cement bond log (CBL) to ensure proper anchoring of the casing to the wellbore.

3.1.4 Online drilling mud gas analysis

Real-time gaseous hydrocarbon monitoring (CH_4, C_2H_6, C_3H_8, i-C_4H_{10}, and n-C_4H_{10}) was conducted during drilling using the ICDP Online Gas Analysis (OLGA) system, which employs a water-gas separator to mechanically extract gases dissolved in the drilling fluid (Erzinger et al., 2006; Wiers-

berg et al., 2020). The extracted gas was continuously transported through a plastic pipe to the analytical laboratory, which was located 15 m from the drilling fluid circulation system. Gaseous hydrocarbons were analyzed every 3 min using a field automatic gas chromatograph (GC-SRI Instruments 86105400) equipped with a flame ionization detector and a hydrogen generator, with hydrogen used as the carrier gas. Gas composition data were recorded at 3 min intervals and correlated with drilling depth using lag depth and penetration rate data. Instrument calibration was performed with standard gases of known concentrations (CH_4: 4870 ppm; C_2H_6: 258 ppm; C_3H_8: 200 ppm; i-C_4H_{10}: 99 ppm; n-C_4H_{10}: 102 ppm), all with uncertainties of $< 2\,\%$.

3.2 Laboratory analyses

3.2.1 Overview of sampling and logging

All drill cores and core catcher samples were shipped to the CSD facility at the University of Minnesota, Minneapolis, Minnesota, USA. Thirty-four scientists from seven different countries visited during a month-long period (August 2024) for initial core description, logging, scanning, and sampling.

All cores were first scanned on a Geotek MSCL-S multisensor core logger for loop magnetic susceptibility, natural gamma, p-wave velocity, gamma density, and electrical resistivity. The cores were then split lengthwise, creating a working half for sampling and an archive half for lithologic description and scanning. The split-core halves were photographed with a Geotek MSCL-CIS digital linescan imaging system and logged on a Geotek MSCL-XYZ multi-sensor core logger for high-resolution point magnetic susceptibility and color reflectance spectrophotometry.

A detailed visual lithologic description was made of the cores. In addition, approximately 5000 samples were extracted at varied intervals through the core sequence for more than 30 types of discrete analyses to be undertaken at collaborators' institutions. A partial list of these ongoing analyses includes geochronology (zircon U / Pb, quartz and feldspar luminescence, weathering (U–Th) / He, ^{10}Be, ^{26}Al, paleomagnetism, bio-chronostratigraphy), biotic composition (pollen, phytoliths, diatoms, ostracods, mollusks), provenance (zircon U / Pb, quartz and feldspar luminescence sensitivity), environmental magnetism, mineralogy (bulk X-ray diffraction (XRD)), scanning electron microscopy (SEM) with energy dispersive X-ray spectroscopy (EDS), inorganic geochemistry (carbonate δ^{13}C, δ^{18}O, and clumped isotopes, X-ray fluorescence (XRF), Nd-Sr isotopes, Li-Si isotopes), and organic geochemistry (total organic carbon (TOC), bulk δ^{13}C of organic matter (OM), biomarkers). Preliminary measurements have been completed for a subset of the samples and a subset of the analyses. We include brief descriptions of primary analytical methods and a summary of available analytical results.

3.2.2 Sedimentology and stratigraphy

Core lithologic description aimed to characterize lithofacies and stratigraphic architecture. Grain size, detrital composition, and sedimentary structures were recorded continuously along the core to establish a detailed facies classification. Facies associations were recognized through the identification of decimeter- to meter-scale grain-size trends and the repeated stratigraphic juxtaposition of specific facies types. Pedogenetic features, including structures and authigenic mineral phases, were documented in detail, along with the identification of recurring pedogenetic overprinting cycles. Trace fossil occurrences and assemblages were also described.

Based on the core descriptions, informal stratigraphic units were delineated according to multi-meter-scale trends in grain size and bed thickness, reflecting broader depositional cycles. Major bounding surfaces were identified and used to define the limits of these stratigraphic units, especially where they coincided with abrupt changes in detrital composition or the onset of distinct pedogenetic features.

3.2.3 Chronology and provenance

Pollen. Over 1000 samples were collected for pollen analysis, focused on facies that were the best candidates for palynomorph preservation but also including the abundant paleosols that rarely preserve palynomorphs. The summary here is based on the processing of 305 samples following standard procedures (Traverse, 2007). The organic matter recovered following standard processing was mounted on 75×25 mm microscope slides. Each slide was scanned using a NanoZoomer N20 whole-slide scanner that digitizes 21 focal planes in each coverslip. These images will be the permanent digital repository of the slides and curated in the Smithsonian's long-term collections. The images were uploaded into OMERO (Open Microscopy Environment) (Allan et al., 2012), a client server environment for managing, viewing, annotating, and analyzing imaging data that are stored on a central server, with a database for the metadata and which can be accessed via a web browser anywhere in the world. The analyst uses those images to detect and identify palynomorphs. We used a two-step process to analyze the images: in the first step, the analyst detects where palynomorphs are in the slide and draws a region of interest (ROI) around the palynomorph. In the second step, the analyst classifies each ROI using a predefined dictionary. We used the morphological database of Jaramillo and Rueda (2025) to identify taxa, which includes all palynological publications from South America, and the biostratigraphic zonation of Jaramillo et al. (2025) to date the sequence.

Detrital zircon U / Pb geochronology. Thirty-two sandstone samples were collected along the drill core for detrital zircon (DZ) U-Pb geochronology, as well as samples from the modern sandbars of the Moa and Juruá rivers nearby the drilling locations to document modern age distributions. Zir-

con was separated from about 250 g of sandstone using conventional hydraulic and magnetic separation at the University of São Paulo. Zircon samples were mounted and analyzed at the University of Arizona LaserChron Center on the Nu instruments HR-MC-ICPMS (inductively coupled plasma mass spectrometer) coupled to a Photon Machines Analyze G2 excimer laser, using a rapid acquisition rate of 300 analyses h^{-1} with a 30 µm spot size (Sundell et al., 2021). We utilized FC-1 as a primary standard, with SL and R33 as secondary and tertiary standards (Gehrels et al., 2008). Ages were filtered to retain only those with $< 15\,\%$ analytical uncertainty. For grains younger than 900 Ma, $^{206}Pb / ^{238}U$ ages were used; for older grains, $^{207}Pb / ^{206}Pb$ ages were used. Additional filters were applied to exclude Proterozoic grains with $> 30\,\%$ discordance or $> 10\,\%$ reverse discordance. Maximum depositional ages (MDAs) were calculated for all samples using the maximum likelihood age algorithm (MLA; Vermeesch, 2021). Systematic and random uncertainties were propagated as detailed in Vasquez and Whiting (2005).

Luminescence dating and provenance. Forty-five samples for luminescence dating and 979 for luminescence provenance were collected for measurements at the University of São Paulo. First, optically stimulated luminescence (OSL) dating of quartz was tested in four samples from the upper 25 m of the core. Quartz and feldspar concentrates were prepared in the 180–250 µm fraction following standard procedures (Mahan et al., 2023). Quartz aliquots (100–300 grains) were measured for equivalent dose estimation using a single-aliquot regenerative dose (SAR) protocol (Murray and Wintle, 2003). Feldspar aliquots from samples at ∼ 4 m depth and ∼ 21 m depth were measured using a post-infrared infrared stimulated luminescence at 290 °C ($pIRIR_{290}$) SAR protocol (Buylaert et al., 2012). Radionuclide (U, Th, and K) concentrations were determined using high-resolution gamma ray spectrometry, and dose rates were calculated according to conversion factors by Guérin et al. (2011).

Luminescence measurements for sediment provenance analysis were carried out in polymineral aliquots (180–250 µm fraction) with the same volume. OSL sensitivity of quartz was measured according to Sawakuchi et al. (2018), which allows the discrimination of Amazonian sediments from Andean and cratonic sources. Quartz OSL sensitivity was measured after infrared stimulated luminescence (IRSL) to bleach feldspar signals. The quartz OSL sensitivity was calculated using the first second of light emission and blue stimulation ($BOSL_{1\,s}$). The $IRSL_{1\,s} / BOSL_{1\,s}$ ratio was used to evaluate the concentration of feldspar relative to quartz in the 180–250 µm fraction, which is a proxy for sand mineralogical maturity.

Heavy mineral analysis and provenance. A total of 160 samples was collected for the analysis of heavy minerals. Partial results were obtained from 26 samples in the lower half of the Acre drill core (505–915 m depth). To extract heavy minerals, the samples were wet-sieved to the 64–180 µm grain-size range, centrifuged in a low-viscosity polytungstate solution (LVP, 2.9 g cm^{-3}), followed by freezing of the heavy minerals fraction and rinsing of the light fraction (Andò, 2020). Heavy mineral glass slides were prepared immersing the grains in Canada balsam for analysis under a polarized light microscope. Quantification is through the identification and counting of 150–300 non-micaceous transparent grains, employing the ribbon counting method (Galehouse, 1971).

Weathering (U − Th) / He geochronology. Four iron-enriched and one ferruginous laterite duricrust were sampled from weathered sediment outcropping in the vicinity of the drilling site and overlaying the Solimões Formation to complement geochronological data on 32 iron-manganese-rich pisoliths or strata from the drill core. For each sample, the material was split in half and photographed, and a subsample was selected for bulk mineralogical and geochemical characterization, as well as micrometric subsamples for (U–Th) / He geochronological analysis. Several aliquots weighing ∼ 50–150 µg were packed into Nd tubes and placed under vacuum for He analysis. Each Nd tube was degassed using a diode laser at temperature < 900 °C during 30 min to retrieve He content and after purification analyzed using a Prisma quadrupole. The tubes were then retrieved from under vacuum and placed individually into a Teflon savilex for wet chemistry digestion. Subsequently, the U, Th, and Sm contents were determined using an ICP-MS at the University Grenoble Alpes (France), using a protocol similar to that of Gautheron et al. (2021, 2022). In this way, the He, U, Th, and Sm content can be used to calculate the (U–Th) / He age for each aliquot with an analytical accuracy of ∼ 3 %.

Cosmogenic nuclides. Samples from the upper portion of the Acre core (∼ 22.7, 39.9, 50.8, and 74.2 m depths) were prepared for measurements of ^{10}Be and ^{26}Al, targeting sediments that were presumed to record sediment deposition ages up to ∼ 5 Ma. Sample preparation included (i) sieving to acquire the 180–1000 µm fraction, (ii) magnetic separation using a Franz system, and (iii) hydrochloric acid (37 %) and oxygen peroxide treatments to remove carbonates and organic matter. These steps were performed at the University of São Paulo. Afterward, the samples were processed at the University of Potsdam (Germany). Quartz purification steps consisted of (i) heavy liquid separation (LST), (ii) seven rounds of 24 h and two rounds of 72 h in H_2SiF_6 : HCl solution, and (iii) one round of 24 h in HF 2 % solution and five rounds of 24 h in HF 1 % solution. The purity of quartz concentrates was tested using ICP-MS measurements. Then, the samples were dissolved in HF 40 % solution for 2 weeks. The HF was extracted, and the samples were dissolved in HCl for isotope fractionation. The isotopic fractionation of the samples is ongoing to isolate Be and Al fractions, with AMS measurements of ^{10}Be and ^{26}Al to be completed at the Helmholtz-Zentrum Dresden-Rossendorf (HZDR) in Dresden, Germany.

Magnetic analysis. Magnetic susceptibility (MS) was measured by two independent methods: (1) along core sections using automated loggers and (2) on oriented individual subsamples. MS data were collected from WR core sections at 4 cm intervals and on the cores at ∼0.5 cm using a Bartington MS3 magnetic susceptibility meter coupled with a Geotek MSCL-S (whole core, MS2C loop sensor) and MSCL-XYZ (half core, MS2E point sensor) at the CSD facility. These values are expressed in 10^{-6} (whole core) and 10^{-5} (split-core) SI units. A total of 119 oriented cubic samples (8 cm^3 each) were collected perpendicular to the core, primarily from fine-grained lithologies, such as mudstone and siltstone. These samples were obtained using non-magnetic knives and saws, stored in acrylic plastic boxes and analyzed at the University of São Paulo. The low-field MS of individual samples was measured using a Kappabridge MFK1-FA system (AGICO) at two frequencies: 976 Hz (low-frequency susceptibility; χLF) and 15 616 Hz (high-frequency susceptibility; χHF) in a 200 A m^{-1} field at room temperature. The χLF and χHF were used to assess the behavior of magnetic grains throughout the χFD% parameter ($\chi FD\% = [(\chi LF - \chi HF) / (\chi LF \times 100)]$) (Dearing et al., 1996). All oriented samples were mass-normalized due to the irregular sample mass inside the cubic boxes, and MS data are expressed in $m^3\ kg^{-1}$.

3.2.4 Geochemistry and mineralogy

Nd and Sr isotopic analyses. Samples of ∼1 g each were collected every ∼20 m (47 total). Samples were processed and analyzed at the University of São Paulo. Samples were first freeze-dried and wet-sieved (63 µm sieve), and then the < 63 µm fraction was centrifuged and oven-dried. The dried material was treated with 10 % HCl, rinsed, centrifuged, oven-dried, and ground with an agate pestle and mortar. Powder samples were dissolved by acid digestion, using HNO_3, HF, and HCl in Teflon beakers at 100 °C. Sr separation was performed using an Sr-specific resin and eluted with 0.05 M HNO_3. Nd was then separated from other rare earth elements first by using the RE resin and then an Ln resin. Sr samples were loaded on single tantalum filament with the addition of tantalum solution ($TaCl_5$). The $^{87}Sr / ^{86}Sr$ isotopic ratios were normalized to the value of $^{86}Sr / ^{88}Sr = 0.1194$. Nd samples were deposited in rhenium parallel filaments with the addition of ultra-pure H_2O. Nd and Sr isotopic ratios were obtained by TIMS using a Thermo Triton. The $^{143}Nd / ^{144}Nd$ isotopic ratios were normalized to $^{146}Nd / ^{144}Nd = 0.7219$ (DePaolo, 1981) and expressed in the ε_{Nd} notation (Jacobsen and Wasserburg, 1980). Uncertainties in $^{87}Sr / ^{86}Sr$ and ε_{Nd} refer to 2 SD and were calculated through multiple analyses. At this stage, 24 samples have been processed and analyzed for $^{87}Sr / ^{86}Sr$ and ε_{Nd}, spanning the whole core and spaced ∼38.5 m from each other.

Inorganic geochemistry and mineralogy. We collected 837 samples of bulk sediment weighing ∼15 g each and spaced ∼1.1 m for magnetic, major elemental, and mineralogical analyses. Due to sample processing techniques, samples were first analyzed for magnetic properties (no sample treatment), then major elements (freeze-drying and grinding), and mineralogy (secondary milling), as described below.

For major elemental analyses, bulk sediment aliquots of ∼5 g were frozen at −60 °C, freeze-dried, and pulverized. The powder was pressed into Chemplex cups with attached thin Mylar foils. Analyses were carried out using a Malvern Panalytical Epsilon 1 X-ray fluorescence (XRF) spectrometer using the Omnian calibration at the University of São Paulo (USP), Brazil, following Kraft et al. (2025). To date, analyses have been completed for the upper 213 samples, representing the upper 267 m below the surface.

X-ray diffraction (XRD) analyses to characterize the qualitative and quantitative mineralogical composition of the sedimentary successions have so far been performed on 100 samples from the upper part of the well, down to a depth of 114 m. The analyses were performed using a Bruker D8 Advance diffractometer with CuKα radiation ($\lambda = 1.54060$ Å), operated at 40 kV and 25 mA, in collaboration with the Center for Mineral Technology (CETEM), Brazil. Samples pulverized for XRF were treated with a subsequent milling step using a McCrone mill to further reduce the particle size to below 10 µm, allowing for quantitative mineralogical analysis through Rietveld refinement with the fundamental parameters approach (Cheary and Coelho, 1992).

Diffractograms were acquired from randomly mounted samples using a step size of 0.02° and a scanning range from 4 to 105° 2θ. Qualitative phase identification was conducted using Bruker DIFFRAC.EVA v6 software, whereas quantitative mineralogical analysis was performed using Bruker DIFFRAC.TOPAS v6. Structures from the International Centre for Diffraction Data (ICDD) and the Crystallographic Open Database (COD) were used in the refinements. For general interpretation, minerals were classified into four main groups: (1) quartz, consisting solely of this mineral; (2) clay minerals plus mica, which include kaolinite, chlorite, smectite, and micas (such as muscovite, biotite, and illite); (3) feldspars, comprising K-feldspar and plagioclase; and (4) carbonates, including aragonite, calcite, and dolomite. Other phases comprise minor components, such as goethite and hematite.

Lithium isotopes. Lithium isotopic measurements (δ^7Li) can be used to infer the history of weathering using the lithium (Li) isotope composition of the detrital sediment, based on a known relationship between chemical weathering intensity in river basins of the present-day Amazon and the isotopic signature of δ^7Li in fine sediments. Forty-seven samples were collected throughout the length of the drill core and were collected in tandem with samples for Nd and Sr isotopic analysis as a constraint on provenance. Analyses are ongoing.

Organic geochemistry. Total organic carbon (TOC) and bulk organic carbon isotopic composition ($\delta^{13}C$) analyses were performed on 30 selected core catcher subsamples, focusing on sediment intervals with the highest potential for organic matter preservation. Analyses were conducted using an Elemental Analyzer Isolink system (Thermo Scientific) coupled to a Delta V Advantage isotope ratio mass spectrometer (IRMS) at the University of São Paulo. Prior to analysis, samples were freeze-dried, finely ground, and subjected to acidification to remove inorganic carbon. Decarbonation was performed through successive additions of 1 mol L^{-1} HCl, with samples maintained in a hot water bath to enhance reaction efficiency. Following acid treatment and drying, samples were weighed into tin capsules, with sample masses adjusted according to estimated carbon content based on preliminary tests.

Biomarker analyses were performed at the University of Southern California on 53 samples spaced roughly every 30 m from representative lithologies including paleosols, fine-grained muds and silts, and sandy horizons. Samples of ~ 60 g were extracted using accelerated solvent extraction and partitioned into hydrocarbon, polycyclic aromatic hydrocarbon (PAH), and fatty acid fractions for biomarker identification and quantification, following standard organic geochemical protocols (see Peaple et al., 2024; Karp et al., 2021).

Methane and carbon dioxide biogeochemistry. During drilling, samples were collected from the top of core sections using sterile tools and immediately stored at −4 °C until further processing. Aliquots of samples were removed for water content and total organic carbon measurements, and the remaining sample was disaggregated. For each depth, four replicates were prepared by adding 10 g of sediment in a 120 mL glass vial, sealed with butyl, and then flushed with N_2 to create an anoxic atmosphere. Incubations were carried out at 25, 35, 50, and 70 °C to simulate thermal gradients associated with sedimentary burial. During the experimental period (up to 30 d at each temperature), headspace samples were collected twice per week using gas-tight syringes (Sawakuchi et al., 2021), and concentrations of CH_4 and CO_2 were determined by gas chromatography (7890A, Agilent Technologies, Santa Clara, CA, USA) at the University of São Paulo.

3.2.5 Biota

Phytoliths. A total of 462 samples were taken for extraction of phytoliths and other biosilica, targeting paleosols, lacustrine sediments, and tuffs (Strömberg et al., 2018), as well as fine-grained sedimentary rock (siltstone, claystone, mudstone, fine sandstone). So far, 330 samples have been processed using standard methods (Strömberg et al., 2018), which include crushing, treatment with HCl to dissolve carbonate cements, sieving to promote deflocculation of the sediment, treatment with Schultze's solution ($HNO_3 + KClO_3$), and floatation with $ZnBr_2$-based heavy liquid, rinsing with ethanol before mounting on slides in Cargille Meltmount. The mounted sample yield was checked for biosilica recovery at 400 × using a Nikon 80i compound microscope. Phytolith morphotypes were identified using Strömberg laboratory protocols (Strömberg, 2003; Stiles et al., 2025), the literature (e.g., Dickau et al., 2013; Crifò and Strömberg, 2021; Morcote-Ríos et al., 2025), and the reference collection of phytoliths extracted from modern plants (1314 taxa) held at the Burke Museum of Natural History and Culture (UWBM), University of Washington, USA.

Ostracods. A total of 138 samples ranging from 10.55 to 913.44 m depth have been washed (dry sample weight between 20 and 140 g) and have undergone a preliminary inspection. From the lower part of the core (depth interval 768.25–913.44 m), 40 samples have been provisionally studied for their taxonomic composition. Eighteen of these samples did not contain any ostracods.

Macrofossils. Thirteen fossils of vertebrate and invertebrate animals were taken in layers distributed from 346.4 m depth to 896.2 m depth. The material was found through visual sedimentological description and has undergone a preliminary inspection for curation and taxonomy at the Federal University of Acre.

DNA geomicrobiology. Samples collected from 66 depths between 4.37 and 921.25 m were analyzed for molecular characterization of the microbial content. However, the difficulty in recovering genetic material in sufficient quantity and quality led to the need for testing multiple DNA extraction protocols. Nine distinct approaches were evaluated, including commercial kits, along with adaptations involving CTAB, phenol-chloroform, and variations in reagent volumes and soil input. Protocols described by Stirling (2003) and Kistler (2011) were also applied, aiming to overcome challenges posed by deep samples, which may contain fragmented DNA or DNA strongly adsorbed to mineral matrixes. Analytical procedures included quantification by Nanodrop and Qubit, agarose gel electrophoresis, and polymerase chain reaction (PCR) using different primer sets.

4 Results

4.1 Drilling

Drilling in the Acre Basin was challenging, and the operation was stopped at a depth of 923 m, short of the original target depth of 2000 m. In total, we retrieved 860.4 m (93 % recovery) of core (Fig. 5).

Multiple drilling problems prevented achieving the target depth. A recurrent issue was the intercalation of unconsolidated sands with strongly consolidated mudstones, which created several obstacles. One was the absence of a stable lithology, originally anticipated at a depth of around 300 m, which was required to anchor the 5.75 in. (146.05 mm) surface casing according to the well engineering plan. Instead,

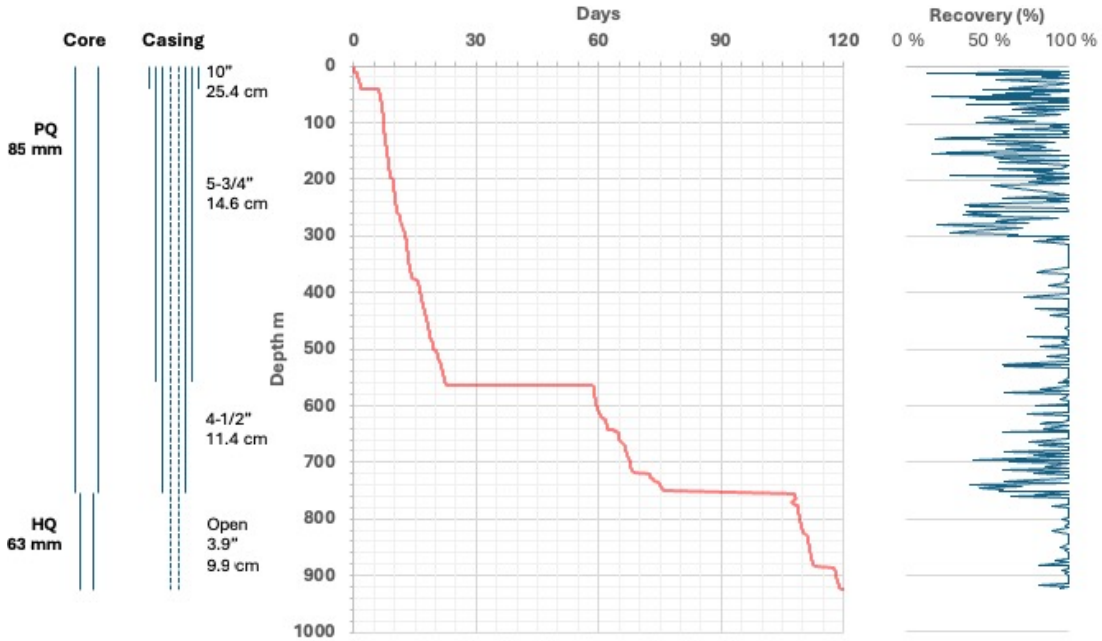

Figure 5. Drilling summary for the TADP-1A well showing (left to right) the dimensions of the core and casing, a time–depth plot, and core recovery.

drilling continued until reaching a relatively consolidated bed at 550 m depth, requiring the installation of an additional 250 m of casing at an additional cost of about USD 150 000. The weight of 550 m of casing, instead of 300 m, likely contributed to the rig failure that resulted in dropping the casing string into the borehole from several meters above the borehole bottom. This issue required an extensive fishing operation to reattach to the dropped casing and downhole logs to confirm casing integrity. The casing installation was completed, cemented, and profiled, and drilling proceeded beyond 550 m depth. The continued occurrence of alternating consolidated and unconsolidated lithologies below 550 m depth led to frequent operational challenges, such as washouts in the sandy beds, localized borehole collapse and swelling clays in the mudstone beds, and differential sticking in coarse units.

At 750 m depth, the drill string became stuck after an unplanned temporary shutdown for rig maintenance. Continued fluid circulation to the surface during attempts to free the string suggested that the cause was differential sticking rather than borehole collapse. Attempts to free the string or cut it above the bottom hole assembly were not successful, and eventually the PQ string was cemented in place as casing for continued drilling with an HQ string and tooling. Coring continued despite increasing problems with the removal of cuttings. Upon reaching 923 m depth in October 2023, a pipe trip was made as part of an attempt to clean the borehole using a tricone bit, but the borehole was blocked at ~ 752–754 m and could not be passed. Caliper logs showed large washouts at this depth, which was cemented to stabilize the borehole. On re-drilling the cement, part of the bottom hole assembly (BHA) was lost, and a fishing tool was subsequently lost in an attempt to recover the BHA. Milling through the lost equipment was unsuccessful, and two attempted sidetracks around the blockage, starting at 695 m and subsequently at 686 m, were both unsuccessful.

To preserve sufficient budget and time for drilling at the second site (Marajó Basin), the TADP Executive Committee made the decision to abandon the hole in December 2023. The cores retrieved in the Acre Basin were transported to the Institute of Geosciences of the University of São Paulo for export to the CSD at the University of Minnesota, arriving in early August 2024. The decommissioning of the Acre drill site and mobilization of the drill rig to the Marajó drill site took place between January and April 2024.

4.2 Field measurements

4.2.1 Field downhole logging

The cement bond log (CBL), acquired with the full-waveform sonic (FWS) tool, showed a good bond between the casing and the borehole wall (bond index) down to 18 m, with a median of 70 %. Below this depth, from 18 to 545 m, the bond was moderate to poor, with a median not exceeding 40 %.

The caliper log (Fig. 6) recorded recurrent washouts ranging from centimeters to meters thick. Thin intervals of washout are likely weak zones associated with the boundary between sandy and fine-grained sediment layers. Thicker washout intervals occurred below 350 m depth, where muddy

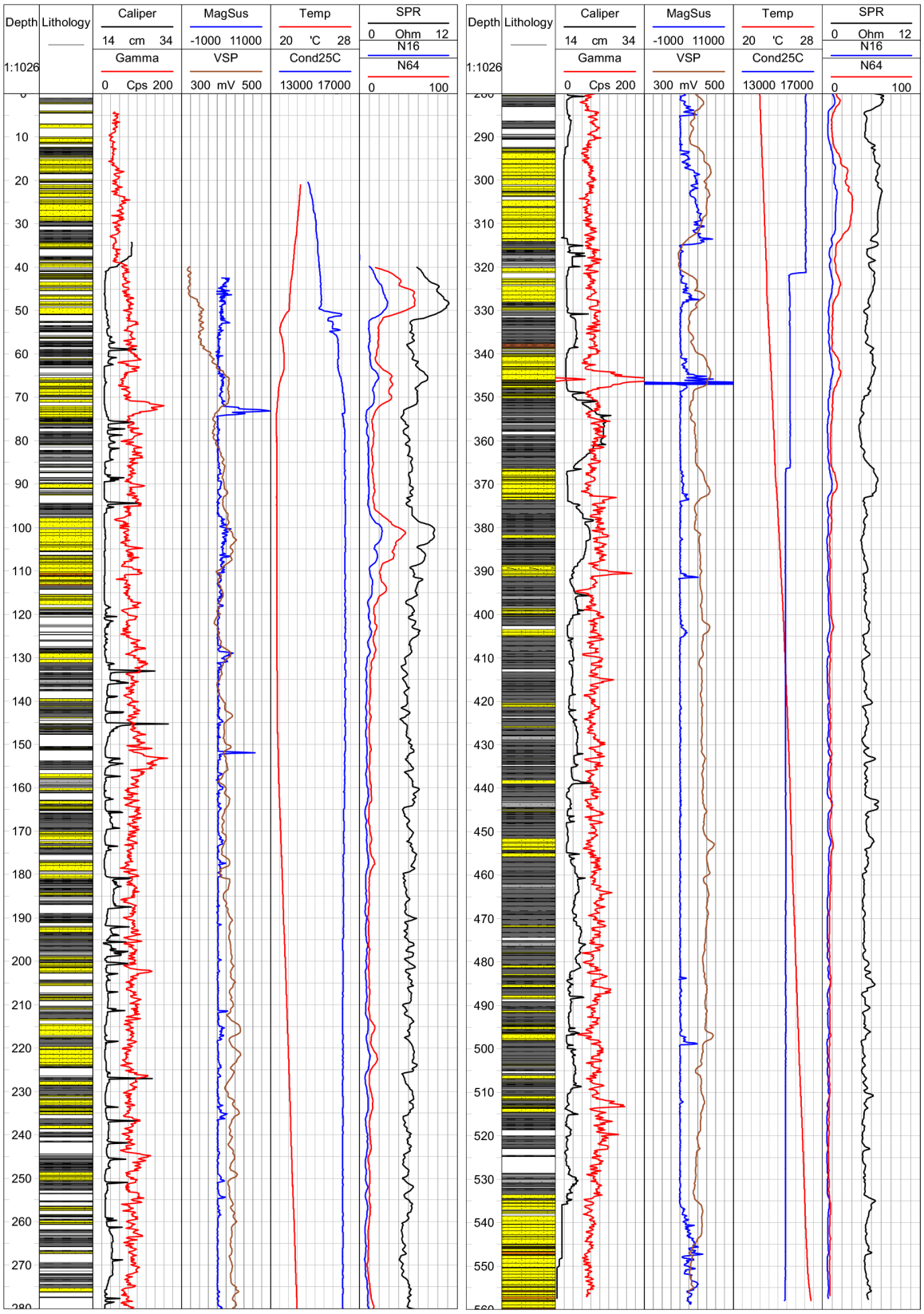

Figure 6. Field geophysical downhole logging of the TADP-1A well showing (left to right) caliper, magnetic susceptibility, temperature, and single-point resistivity (SPR) measurements relative to lithology in the upper (left half) and lower (right half) portions of the drill hole. Lithologic units are the same as in Fig. 7.

sediment layers became more continuous. In general, the thickest washout intervals were observed in clay-rich sections.

In general, the natural gamma log (Fig. 6) shows a good correlation with the recorded stratigraphy, increasing in more clay-rich sections and decreasing in sandy intervals. However, this pattern was inverted in the intervals of 23.5–51 m, between 38 and 52, 70–75, and 389–391 m. The readings are significantly structured, displaying several major peaks (e.g., 72–74, 153–155, 344–347, 373, 390–391 m depth) and several lesser peaks (e.g., 202–203, 226–227, 245–246, 415, 513 m). Most of these peaks coincide with natural gamma peaks also recorded during laboratory measurements of whole cores on the MSCL (Fig. 7), which allows core-hole data comparisons. In some cases, downhole natural gamma peaks coincide with downhole magnetic susceptibility peaks (e.g., 72–74, 344–347, 373 m), with increases of two to three times, indicating a strong correlation when variations exceed 3 SI units in the magnetic susceptibility profile, although this relationship is somewhat clearer in the laboratory logging results.

The electrical logs from the GRP1000 tool showed some sections of higher permeability, indicated by a greater inflection in the single-point resistivity (SPR) and spontaneous potential (SP) curves, and a separation between the short and long resistivity curves in the intervals between 63–73, 95–110, 293–315, 319–329, 339–350, and 366–375 m. Additionally, the SPR log generally showed a response that aligned well with the lithological variations described from the cores and can be used to aid in the interpretation of sections with low core recovery or a gap.

A comparison of the fluid temperature and conductivity logs with the electrical logs shows two inflection points in the curves – one at 321 m and another at 366 m – which coincide with sections of higher permeability.

The FWS log showed good correlation with major changes in lithology, indicating a high-quality performance of the tool. In most of the profile, it was possible to identify both compressional (P) and shear (S) waves. These data will be very useful for future, more detailed analyses to determine the mechanical properties of the material and to estimate porosity, following calibration with core scan data.

4.2.2 Gas composition in the drilling mud

The gas composition in the drilling fluid from the well is dominated by CH_4, with lower concentrations of C_2H_6, C_3H_8, and n-C_4H_{10}. OLGA measurements identified CH_4-rich zones at depths of 250–380 and 420–588 m, where C_2H_6 and C_3H_8 also show notable peaks. In contrast, i-C_4H_{10} and n-C_4H_{10} concentrations are lower in these intervals but increase between 600 and 700 m. CH_4 shows weak correlation with C_2H_6 ($\rho = 0.34$), C_3H_8 ($\rho = 0.38$), i-C_4H_{10} ($\rho = 0.43$), and n-C_4H_{10} ($\rho = 0.43$), whereas C_2H_6 and C_3H exhibit a strong correlation ($\rho = 0.85$). Spearman correlations (ρ) are considered significant when $p < 0.05$, although in this case, $p > 0.05$, which suggests no strong statistical significance, as reported in Martinez et al. (2025).

The stable carbon isotope analysis of eight CH_4 samples from the gas line yielded $\delta^{13}C$ values ranging from −35 ‰ to −25 ‰. In the depth interval between 474 and 514 m, $\delta^{13}C$ values were below −27 ‰ (Martinez et al., 2025). Additionally, the 300–314 m depth range had more negative $\delta^{13}C$ values compared to other intervals. Additional data on downhole gas analyses are available in Martinez et al. (2025).

4.2.3 Pore-water sampling

Pore-water values for $\delta^{18}O$ ranged from −6.11 ‰ to −4.88 ‰, and from −38.1 ‰ to −30.5 ‰ for δ^2H, with a gradient of 5.7 and an intercept (deuterium excess) of −3.1. The shallowest sample (19.4 m depth) is on the depleted end, with $\delta^{18}O$ of −6.11 ‰ and δ^2H of −37.2 ‰. Values increase with depth up to 60 m (−5.44 ‰ and −33.9 ‰), decrease to 140 m (−6.10 ‰ and −38.1 ‰), and increase again down to 630 m (−4.88 ‰ and −30.5 ‰). Intercept and deuterium excess for local rainwater values, established for Cruzeiro do Sul (10 km north of the drilling site) by Martinelli et al. (1996), are significantly different. The gradient is 8.18, similar to the Global Meteoric Water Line (GMWL) value of 8, and deuterium excess is 15.1, higher than the GMWL value of 10. Individual sample values were unfortunately not shown by the authors. The differences between local precipitation and the GMWL are caused by the evaporative cycles that rainwater undergoes during transport from the Atlantic Ocean to the studied region (Gat and Matsui, 1991; Martinelli et al., 1996). The lower gradient and deuterium excess for pore water is probably caused by water–rock interaction.

The isotopic signature of the water well samples (up to 80 m deep) overlap with the pore-water values, being closer to the more depleted end of their range: −6.04 ‰ to −5.57 ‰ for $\delta^{18}O$, and from −37.2 ‰ to −34.5 ‰ for δ^2H. The Juruá River sample is the most enriched water we analyzed, with −2.93 ‰ for $\delta^{18}O$ and −19.0 for δ^2H. The values for shallow piezometers and the spring water overlap with part of the pore-water samples, extending to more enriched values, with $\delta^{18}O$ ranging from −5.63 ‰ to −3.96 ‰ and δ^2H ranging from −35.9 ‰ to −23.1 ‰. Since these samples were collected during a single season, the influences of seasonality cannot be evaluated, and new samples will be collected for that purpose. The drilling mud sample values fall within the pore-water range, with −5.89 ‰ for $\delta^{18}O$ and −36.8 ‰ for δ^2H, making isotopes a less effective tool to determine contamination.

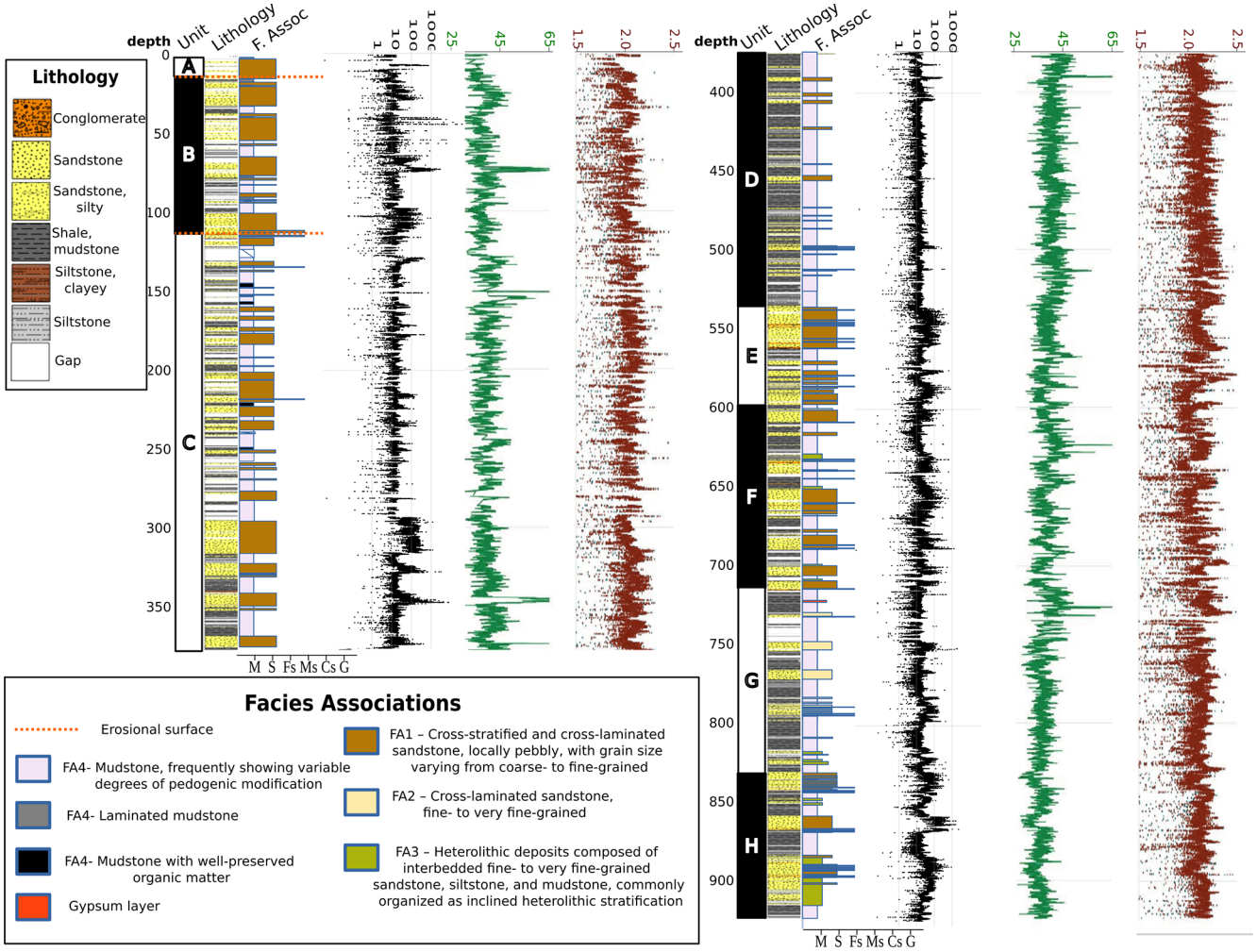

Figure 7. Core-based sedimentological and geophysical logs. The left panel spans from the top to the base of Unit C, whereas the right panel extends from the top of Unit D to its base. In both panels, the leftmost column shows the proposed informal lithostratigraphic units (A–H), together with the lithological profile and facies associations (see in-figure captions). Grain-size classes are abbreviated as follows: M, mud; S, silt; Fs, fine sand; Ms, medium sand; Cs, coarse sand; G, granules. Multi-sensor core logger data are plotted alongside the lithological logs. From left to right: magnetic susceptibility (black; SI units, $\times 10^5$), natural gamma radiation (green; counts per second, CPS), and gamma density (red; g cm^{-3}). Core depth scales were generated by applying a linear compression factor for core runs to fit the drilled interval when recovery was > 100 % (equivalent to the CSF-B depth scale used in scientific ocean drilling, e.g., Expedition 337 Scientists, 2013).

4.3 Multi-sensor core logging

There is significant coincidence between the downhole and core natural gamma peaks; however, there is considerably more structure evident in the core data. From a qualitative perspective, the core natural gamma (Fig. 7) has two different types of maxima: seven very narrow high-amplitude "spikes" (the comprehensive list of spikes have maxima at 73, 155, 346, 373, 390, 623, and 726 m) and far more numerous, broad lower-amplitude "peaks" (a few examples of such "peaks" include those with maxima around 25, 333, 361, 379, 646, 671, and 691 m). Four of the natural gamma spikes, at 73, 346, 373, and 390 m, coincide with magnetic susceptibility spikes, while the remaining three gamma spikes, at 155, 623, and 726 m, have no corresponding magnetic susceptibility increase. The highest amplitude gamma spike is found at 346 m, with natural gamma values above background over a ~ 4 m interval (348.06–344.23 m) and a sharp maximum at 346.27 m. This natural gamma spike coincides with a sharp peak of magnetic susceptibility. We suspect that these gamma spike intervals consist of altered volcanic ashes and are undertaking further mineralogical, petrologic, and geochemical studies of these targets. Meanwhile, the broader natural gamma "peaks" usually have no accompanying MS maxima, and we suspect that these may be recording potassium-rich, iron-poor, fine-grained sediment, a surmisal that will be tested with scanning XRF data.

The MS core logging data are more richly structured than both the downcore MS logging data and the laboratory natural gamma data just discussed. The MS core log exhibits many significant peaks that generally correspond with sandy units that likely contain significant amounts of magnetite and ilmenite in their heavy mineral fraction. Unlike the positive correlation between natural gamma and magnetic susceptibility observed for the gamma "spikes", most of the broad MS peaks coincide with broad natural gamma minima. Some examples of the latter include the intervals between 99–109, 535–560, 856–867, and 884–906 m. The natural gamma minima imply a dearth of K, U, and Th-bearing minerals such as K-feldspars and clay minerals. There is both a notable increase in the thickness of MS peaks in the lower half of the core (below 530 m) and an increase in the magnetic susceptibility background values (below 740 m).

4.4 Sedimentology

The entire described section comprises fine to medium arkosic or non-arkosic sandstone, siltstone, and mudstone (Fig. 7), exhibiting varying degrees of paleopedogenetic alteration. In layers where weathering is minimal, the sand-grade facies are rich in feldspar grains and lithic fragments, displaying a grayish coloration that contrasts with the reddish oxidized hues and local green mottling found in the more intensely paleo-weathered profiles. Four facies associations (Fig. 8) characterize the sedimentological features that developed during deposition.

Facies association 1 (FA1) consists of fining-upward sandy successions that range from 2 to greater than 10 m in thickness. These successions typically rest on sharp erosional surfaces overlain by coarse sandstone (primarily arkosic) or conglomerates, which mainly contain intraclasts, particularly mud clasts and reworked fragments of carbonate nodules and concretions. Extra-basinal granules and small pebbles are present only in the uppermost stratigraphic intervals, as described in the stratigraphy subsection below. These coarse sandstones and conglomerates transition upward into cross-stratified medium to fine sandstone, which rarely contain scattered intraclasts and plant fragments. Additionally, planar-stratified and structureless sandstones are also present. Post-depositional alteration and obliteration of the original sedimentary structure due to paleopedogenesis is common.

Facies association 2 (FA2) is characterized by fine to very fine cross-laminated arkosic or non-arkosic sandstone, featuring centimeter-scale stoss-erosional sets that create uniform successions up to 1.5 m thick.

Facies association 3 (FA3) consists of centimeter-scale intercalations of fine to very fine cross-laminated arkosic or non-arkosic sandstone, laminated siltstone, and mudstone. These materials are often arranged in inclined heterolithic successions that can reach thicknesses of up to 1.5 m.

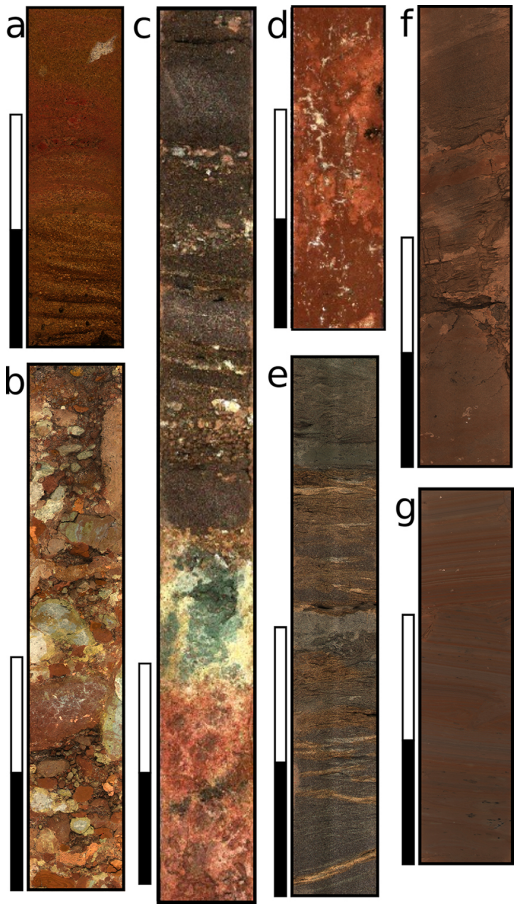

Figure 8. Representative pictures of the proposed facies associations: **(a)** quartz-rich conglomerate from FA1 (Unit A), showing cross-stratification and thinning upward graining; **(b)** intraclast conglomerate from FA1 (Unit C, clasts are mainly mudclasts and carbonate nodules); **(c)** blocky paleosol displaying reduction halo below contact with conglomeratic sandstone from FA1 (Unit C); **(d)** blocky paleosol with drab haloed root traces and carbonate concretions, developed on FA4 deposits (Unit C); **(e)** fine to very fine cross-laminated sandstone from FA2 (Unit G); **(f)** inclined heterolithic succession from FA3, comprising laminated siltstone, coarsening upward to very fine cross-stratified sandstone interbedded with mudstone (Unit E); and **(g)** laminated claystone beds from FA4 with minor plant debris (Unit C).

Facies association 4 (FA4) is characterized by laminated claystone and minor laminated siltstone, which rarely contain preserved organic matter, plant fragments, and mollusk shells. Organic mud layers that have been preserved from oxidation are limited and typically do not exceed 1 m in thickness. Thick examples of FA4 occur at only three specific stratigraphic positions (as detailed below).

The four facies associations compose fining-upward cycles that range from 5 to over 25 m in thickness. These cycles are interpreted as the preservation of fluvial channel and bar deposits transitioning into fluvial bar tops and floodplain deposits. The direct transition from FA1 to FA4 is the most

common occurrence, while the preservation of all four facies associations within a single cycle is rare. Additionally, the local accumulation of muddy successions reaching thicknesses of up to 10 m and often transformed into stacked paleosol sequences is interpreted as periodically exposed, well to moderately well-drained, settling-dominated floodplain deposits.

These depositional sequences are overprinted by paleopedogenetic alteration that primarily affects the fine-grained deposits but also can extend to sandy facies, depending on the thickness of the floodplain and bar-top successions. Paleosols are characterized by changes in color, mottling, oxidation, carbonate nodules and concretions, rhizoconcretions, and local granular and blocky peds, as well as slickenside structures and sand-filled fractures. The deepest stratigraphic levels (below 712 m depth) also contain sometimes-abundant gypsum. Paleosols are present throughout the entire succession and consist of meter-scale units with poorly to well-defined individual B and C horizons, while some areas retain A horizons. Centimeter-scale meniscate burrows, primarily classified as *Taenidium* isp., are commonly observed.

4.5 Lithostratigraphy

Apart from the uppermost 12 m, the entire sampled section can be attributed to a single lithostratigraphic unit that we identify as the Solimões Formation. However, the unit can be subdivided based on the relative abundance of sandy fluvial channel deposits (FA1 and FA2) and finer-grained deposits (FA3 and FA4). Seven informal subdivisions were designated with letters (Fig. 7) to facilitate description and correlation with biostratigraphic and chemostratigraphic data. Smaller-scale fining-upward cycles, which can be up to 25 m thick, were likely formed by the migration of fluvial channel belts within the basin and are not expected to represent regionally correlative stratigraphic units. On a broader scale, three major stratigraphic surfaces were identified that could be useful for regional correlation. A larger order surface, which bounds two large-scale coarsening-upward cycles, is located at the depth of 536 m. A major erosional surface marks a change in the composition of pebbles and granules, with the first appearance of extra-basinal clasts, predominantly volcanic, occurring at the depth of 110 m, in the upper part of the second coarsening-upward cycle. At the depth of 12 m, another erosional surface indicates a further change in the composition of granules and pebbles, this time reflecting a dominance of quartz fragments. Below the major cycle-bounding surface, the first coarsening-upward cycle consists of four distinct units. The first unit, informally designated as Unit H, extends from the base of the core at 923 m to the depth of 831 m. It is characterized by an abundance of muddy paleosols containing authigenic crystals preliminary identified as gypsum, interbedded with successions of predominantly fine sandstone from FA2 and local FA1, with thin layers of pebble intraclast conglomerate that occasionally contain wood and bone fragments. The second unit, named Unit G, extends from the depth of 831 to 712 m and is characterized by muddy paleosols containing gypsum crystals, with scattered fine-sand intercalations that are rarely thicker than 2 m. The third unit, referred to as Unit F, spans from depths of 712 to 598 m and is composed of sharp-based fining-upward cycles that can reach thicknesses of up to 25 m. Each cycle begins with fine sandstones from FA1, gradually transitioning into FA4. The paleosol horizons in Unit F and above are devoid of gypsum. Unit E occurs between depths of 598 and 534 m, and is composed of sandy and pebbly facies associations (FA1 and FA2), also organized into erosional-based fining-upward cycles.

At the depth of 534 m, an abrupt return to the dominance of facies associations FA3 and FA4 marks a major surface bounding the two large-scale coarsening-upward cycles. The first unit of the second cycle, Unit D, extends from depths of 536 to 374 m and is characterized by several fining-upward cycles, each up to 15 m thick. These cycles begin with intervals of FA1, typically less than 2 m thick, consisting of fine sand that is devoid of mud or calcite intraclasts, and culminate in thick successions dominated by FA4. Continuous successions of fine-grained facies and oxidized muddy paleosols reach up to 15 m, with fine-grained facies being more abundant than sandy facies in this unit. Unit C occurs from depths of 374 to 110 m and marks the overall coarsening-upward trend of the second cycle, displaying thicker sandy intervals within its fining-upward successions. These typically consist of 3 to 9 m thick successions of fine to medium sandstone with intraclast conglomerates near their bases. Muddy paleosols remain dominant in Unit C, and units C and D are the only stratigraphic intervals where organic muds preserved from weathering were found, specifically at depths of 145, 246, and 488 m. Unit B extends from depths of 110 to 12 m and rests atop a major erosional surface that marks the onset of local input of pebbles and granules of volcanic composition from sources outside the basin. The overall stacking pattern of the smaller fining-upward successions indicates the continuation of the second coarsening-upward cycle, accompanied by a reduction in the thickness of the fine-grained beds to just a few meters each.

From a depth of 12 m to the surface, a single fining-upward cycle is observed, consisting of a lower conglomerate with quartz pebbles, quartz-rich sandstone, and red uncompacted weathered muds. This cycle rests on another major erosional surface. The notable shift from the feldspar-rich composition of the sandy facies below indicates that this upper interval does not belong to the Solimões Formation but rather represents a younger unit of indeterminate age.

4.6 Chronology/provenance

4.6.1 Pollen

Among the 306 samples that have been processed to date, 155 are sterile, and 151 have some degree of organic mat-

ter recovery. The analysis of 65 samples, with an interval of 15 m between each sample, has been completed. A total of 102 820 grains have been detected, with identifications for 39 472 of these. Sample counts range from 2 to 14 230 grains per sample, with a mean of 720 grains per sample. Palynomorphs have been detected from 54.7 to 913 m, but the palynomorph classification has only been done in 38 % of the grains. Sterile intervals include 18–57, 154–210, 406–482, 487–511, and 591–629 m. The overall palynological recovery from 631 to 913 m was higher than from 0 to 631 m. Key biostratigraphical occurrences include the *Cyatheacidites annulatus* FAD (first appearance datum) at 512 m, the absence of *Crassoretitriletes vanraashdooveni*, the LAD (last appearance datum) of *Grimsdalea magnaclavata* at 154 m, the LAD of *Retibrevitricolporites yavarensis* at 548 m, and the LAD of *Echiperiporites intectatus* at 788 m. The assemblage suggests that the upper 512 m is not older than 6 Ma (the hiatus and SOL-17 zones of Jaramillo et al., 2025). The interval 913–512 m could belong to zone SOL-15 and the upper SOL-14 (6 to ∼ 10 Ma), but presently there are too few samples with taxonomic classifications in this interval.

4.6.2 Detrital zircon U / Pb geochronology

Results from six samples are included, including modern sand from the Juruá River near the well site and five sand/sandstone samples collected at 1, 178.5, 300.1, 497.4, and 863.0 m. Between 387 and 584 zircon grains were analyzed per sample to increase the chance of identifying neo-volcanic zircons, even if they constituted a minor proportion of the grains from the source areas. A seemingly robust maximum depositional age (MDA) estimate of 5.8 ± 0.21 Ma for sample 1A100Q2 at 178.5 m depth is based on 18 young grains. Remarkably, no ages younger than ∼ 6 Ma are found up-section, nor do they occur in the modern sand of the Juruá River, either reflecting the absence of volcanism since the latest Miocene in the source areas to the west along the northern Peruvian Andes or reduced deposition of latest Miocene to late Quaternary sediments in this part of the Acre Basin. Down-section, MDA estimates increase to 7.8 ± 0.5 Ma (300.1 m), 8.6 ± 0.2 Ma (497.4 m), and 11.8 ± 0.4 Ma (863 m). Thus, our current MDA results suggest that strata at the bottom of the well (923 m) were likely deposited around 12 Ma or somewhat younger. Detrital zircon age populations are multi-modal and remarkably similar in all samples, with a dominant Permo-Triassic age population. A control sample collected in a modern sand bar of the Juruá River ($n = 437$), close to the drilling location, shows similar age distributions, albeit with the appearance of a Jurassic population, an increase in the Cenozoic age peak, and a reduction in the Permo-Triassic population (Fig. 9). Our age constraints allow us to unambiguously document a dominant Andean contribution to the sedimentary budget accumulated in the Acre Basin in the recovered sequence, although the data do not entirely preclude the possibility of the recycling of Andean sediments that were previously deposited upstream in the Acre region.

4.6.3 Luminescence

Preliminary results indicate that quartz natural OSL signals are saturated for two samples tested: one at 1.3 m and the other at 10 m depth. Minimum equivalent doses are 135 ± 8 Gy ($n = 9$) and 180 ± 13 Gy ($n = 5$), based on the double of the characteristic dose ($2D_0$). Hence, quartz OSL dating provides only minimum sediment deposition ages. Given the dose rates of 1.51 ± 0.09 and 1.91 ± 0.12 Gy ka^{-1} for quartz, the samples at 1.3 and 10 m depth would correspond to minimum ages of 89 and 94 ka, respectively. Feldspar natural $pIRIR_{290}$ signals were also in saturation for samples at 4 and 21 m depth, indicating minimum equivalent doses of approximately 600 Gy. Average values of $2D_0$ for the $pIRIR_{290}$ was 616 ± 14 Gy ($n = 5$) for the 4 m depth sample and 630 ± 36 Gy ($n = 5$) for the 21 m depth sample. The residual doses of up to 100 Gy may occur in $pIRIR_{290}$ signals from fluvial sediments in the Amazon, and, thus, true equivalent doses may be approximately 500 Gy here. Considering the $2D_0$ of 630 Gy and dose rates of 3.19 ± 0.18 Gy ka^{-1} for feldspar, the sample at 21 m depth would correspond to a minimum age of 198 ka. Thus, both quartz OSL and feldspar $pIRIR_{290}$ dating suggest that sediments in the upper portion of the core were deposited beyond ∼ 200 ka.

Quartz OSL sensitivity ($\%BOSL_{1\,s}$) in polymineral aliquots is relatively low, ranging from 3 % to 7 % in the interval from 15 to 923 m depth. The 580–640 and 750–923 m depth intervals show sediment layers with $\%BOSL_{1\,s}$ reaching 6 %–7 %. Brighter quartz grains are observed only in the upper 10–15 m depth, with $\%BOSL_{1\,s}$ in the 15 %–30 % range. The $IRSL_{1\,s}$ / $OSL_{1\,s}$ ratio indicates sands rich in feldspar, except for the upper 15 m, which has a low feldspar content. In summary, preliminary luminescence analysis indicates the dominance of immature feldspar-rich sands supplied from sources with high denudation rates, similar to Andean sands transported by the Solimões and Madeira rivers (Sawakuchi et al., 2018). The upper 10–15 m has higher maturity sands, with quartz grains supplied by lower denudation rate sources, possibly from recycled Andean sediments or a mixture between Andean and cratonic sources.

4.6.4 Heavy minerals

Heavy mineral samples from the Acre drill core contain a variety of minerals, which include epidote, zircon, rutile, tourmaline, garnet, kyanite, andalusite, sillimanite, enstatite, hypersthene, hornblende, augite, and diopside. The initial results of quantification of the heavy minerals assemblage allow for a preliminary picture of the heavy mineral composition in the lower half of the Acre drill core. Clinopyroxene concentration (mostly augite and diopside) ranges from 7 % to 24 %, whereas orthopyroxene (hypersthene and enstatite)

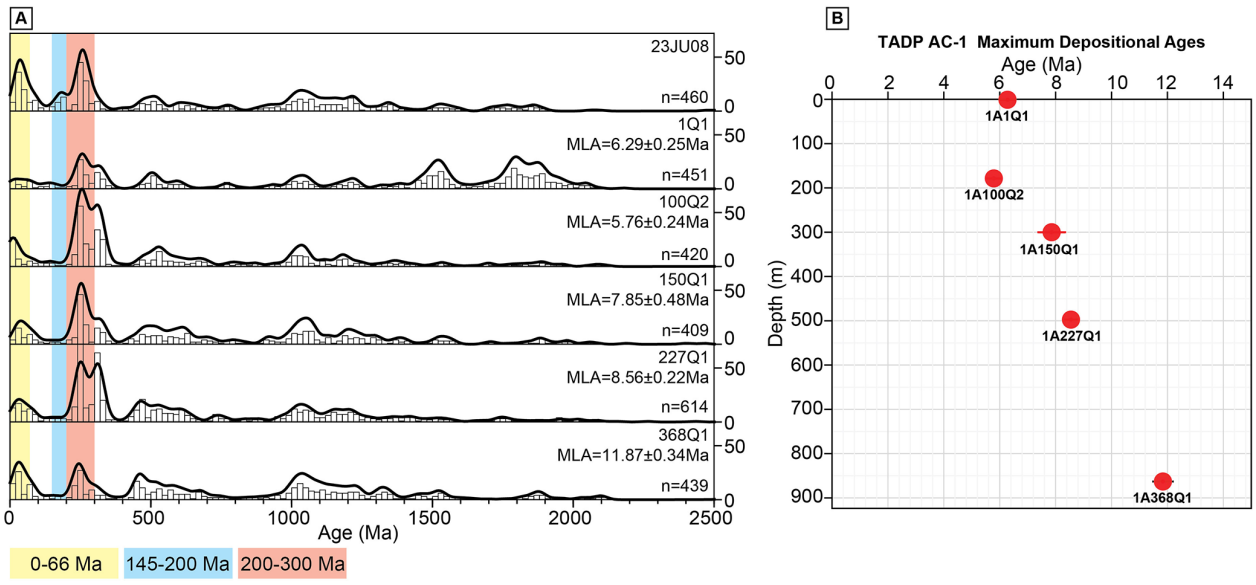

Figure 9. Detrital zircon U-Pb age distributions and maximum depositional ages for well TADP-1A: **(A)** kernel density estimates (black lines) and histograms (gray bars) of detrital zircon U-Pb ages for selected stratigraphic depths. Colored bands highlight key age ranges: Cenozoic (0–66 Ma, yellow), Jurassic (145–200 Ma, blue), and Permian-Triassic (200–300 Ma, red). Reported maximum likelihood age (MLA) and number of analyses (*n*) are shown for each sample. **(B)** Maximum depositional ages (red circles) plotted as a function of depth for the same samples.

concentrations are comparatively higher, ranging from 2 % to 30 %, with a majority of samples exceeding 20 %. Both populations show no clear variation in the concentration along the core extent. Hornblende concentration shows significant variation, ranging from below 5 % up to 60 %, with a tendency of enrichment toward the major erosional surface at the 536 m depth. Aluminosilicates (mostly andalusite and staurolite, with minor kyanite) often sum up to 5 % to 10 % of the heavy minerals, with a few exceptions surpassing 12 %, trending below 5 % toward the 536 m erosional surface. Garnet grains, similarly, have abundances often in the 5 % to 10 % range from the base, trending under 5 % toward the 536 m depth. Ultra-stable minerals (zircon, rutile, and tourmaline) account typically for values around 20 % of the samples, with a few exceptions slightly surpassing 30 %, with a gradual impoverishment (down to 5 %) toward the 536 m erosional surface.

Although the heavy mineral results are still preliminary in nature, they show some gross trends of heavy mineral compositional change along the lower half of the Acre drill core. The relatively abundant assemblage rich in augite, hypersthene, and hornblende resembles the heavy mineral assemblages found in the modern Amazon River channels (Nascimento et al., 2015), suggesting that most of the provenance sources are from basic igneous rocks from the Andean Range. The less frequent contribution from aluminosilicates and ultra-stable minerals suggests that low- to medium-grade metamorphic rocks, and even plutonic rocks, may play a minor role in the sediment sourcing. These minor sources have a progressively lower presence toward the erosional surface at the 536 m depth, indicating a prevalent and growing component of Andean sources from the bottom of the Acre drill core up to the middle of the drilled sequence.

4.6.5 Cosmogenic nuclides

ICP-MS data demonstrate that the cosmogenic samples were successfully purified, and quartz grains were isolated. Despite significant material loss during physical separations and acid treatments, enough material remained for dissolution and chemical fractionation (25 to 46 g). Due to the naturally low Be content in the sediments, a known amount of ^{10}Be (approximately 0.23 mg) was added to each sample. After undergoing the chemical separation steps of hydroxide co-precipitation (to remove Mg, Mn, K, and Ti) and isotopic fractionation columns for Fe, Be, and Al, high recovery rates of Be (85 %–92 %) and Al (89 %–99 %) fractions were recorded relative to the total sample aliquot. The results indicate that the samples from the first 75 m, even with relatively small masses for in situ cosmogenic nuclide analysis in basins with low isotopic production rates (such as the Acre Basin), are promising for the use of the ^{10}Be and ^{26}Al pair in analyses.

4.6.6 Magnetic measurements

Magnetic susceptibility remains positive throughout the entire TADP-1A core (Fig. 10). Furthermore, magnetic susceptibility measurements taken along core sections

and on oriented samples exhibit good agreement. The magnetic susceptibility of oriented samples ranges from 5.60×10^{-8} to 7.60×10^{-7} $m^3\,kg^{-1}$, with an average value of 1.50×10^{-7} $m^3\,kg^{-1}$. The highest MS values are observed in the lower portion of the core, at a depth of approximately 750–800 m. MS values are lower toward the top of the core, reaching a minimum at a depth of 1.7 m. The high positive MS values suggest a main contribution of paramagnetic and/or ferrimagnetic minerals. Based on the χFD% values, there is a predominance of particles with values lower than 4 % at the base of the core, indicating a prevalence of larger grains, characterized as MD (multi-domain) or PSD (pseudo-single domain) particles. Above 350 m depth and toward the top section, the χFD% values increase to above 5 %, suggesting a primary contribution from SP (superparamagnetic) grains. Some significant variations, or peaks, may indicate changes in sedimentation rates or the presence of different magnetic minerals within the core. Further magnetic analyses will be conducted to determine the magnetic carriers and their specific characteristics.

4.6.7 Nd and Sr isotopic analyses

ε_{Nd} values vary between −11.1 and −9.9 (average -10.5 ± 0.7 (2 SD)). ε_{Nd} values generally decrease from the bottom to the top of the record, but this trend is not statistically significant with the current analytical results. $^{87}Sr / ^{86}Sr$ values vary between 0.7187 and 0.7312 (average 0.7232 ± 0.0062 (2 SD)). $^{87}Sr / ^{86}Sr$ values are relatively low from the bottom of the record until ∼ 525 m depth, increase until ∼ 300 m depth, decrease again until ∼ 45 m depth, and increase, reaching the maximum values in the uppermost two samples of the record.

In general, ε_{Nd} and $^{87}Sr / ^{86}Sr$ values form a narrow cloud of points within the typical values reported for the eastern tropical Andes, the Altiplano, and the tropical Subandean foreland (Pinto, 2003). As a result, they coincide with the expected values for a mixture of suspension sediments from the Solimões and Madeira rivers (Allègre et al., 1996; Viers et al., 2008; Bouchez et al., 2011; Höppner et al., 2018), the two main Andean tributaries of the Amazon River, and are in agreement with suspension sediments found at the mouth of the Amazon River, as well as offshore from the mouth (Zhang et al., 2015; Höppner et al., 2018).

4.6.8 Weathering (U–Th) / He geochronology

The outcropping layers with ferruginous clasts from four sites consist mainly of a hematite phase with residual quartz grains, while the Fe-lateritic duricrust sample is composed of a hematite layer rich in kaolinite and a pure goethite layer. Each mineralogical phase was dated, and preliminary (U–Th) / He data were obtained only from the hematite in the iron-enriched samples and the goethite layer in the Fe-lateritic duricrust. Notably, all aliquots yielded systematic Quaternary ages, with values ranging from approximately 0.4 ± 0.2 to 1.0 ± 0.5 Ma, although with large uncertainties due to low helium content. Despite the significant errors in these preliminary data, all ages fall within the Quaternary period, and no age difference was detected between the stonelines and the Fe-lateritic duricrust samples. However, the chemistry of these samples differs markedly: the stonelines (hematite) exhibit U concentrations of 1 to 6 ppm and Th concentrations of 5 to 23 ppm, whereas the goethite extracted from the Fe-lateritic duricrust shows U concentrations similar to those of hematite (3–8 ppm) but significantly lower Th concentrations (1–2 ppm). Additional data are currently being acquired to refine and improve the accuracy of the (U–Th) / He ages, but we can now conclude that the host sedimentary formation is older than 1 Ma. Where Fe-clasts from the TADP-1A core were examined and found to contain porous mixed Fe-Mn oxide phases, the purest samples were prepared for ongoing (U–Th) / He dating.

4.7 Geochemistry

4.7.1 Inorganic geochemistry and mineralogy

Among the many major elemental ratios, we report ln(Al / Si) and ln(Fe / K), because of their strengths and applicability to track sources of sediments transported by Amazon fluvial systems (Bouchez et al., 2011; Govin et al., 2012; Zhang et al., 2017; Grigolato et al., 2025). Minimum and maximum ln(Al / Si) values are −2.72 and −1.03, respectively, whereas the average value is −1.43. The ln(Al / Si) values are relatively stable throughout the analyzed portion of the record, with three notable excursions toward lower values: (i) between ∼ 111 and ∼ 99 m below the surface; (ii) between ∼ 77 and ∼ 63 m depth; and (iii) between ∼ 55 and ∼ 38 m depth. Minimum and maximum ln(Fe / K) values are −0.70 and 1.49, respectively, while the average value is 0.56. The behavior of the ln(Fe / K) values is similar to that of the ln(Al / Si), but ln(Fe / K) values show two additional excursions toward lower values, namely between ∼ 228 and ∼ 214 m depth and between ∼ 30 and 15 m depth.

While ln(Al / Si) can be considered a proxy for grain size (the smaller the grain size, the higher the ratio) for sediments from the Amazon rivers (Bouchez et al., 2011; Sun et al., 2017), ln(Fe / K) has been used as a proxy for distinguishing Andean versus lowland sources of sediments (the more Andean sediments, the lower the ratio) (Bertassoli et al., 2019; Grigolato et al., 2025), as well as changes in the strength of chemical weathering of sediment sources (the stronger the chemical weathering, the higher the ratio) (Zabel et al., 2001; Govin et al., 2012). Because the Andes seems to be the primary source of sediments (see results from various proxies), ln(Fe / K) may be primarily controlled by chemical weathering. The three excursions toward lower ln(Al / Si) and ln(Fe / K) values suggest the occurrence of coarser less-weathered sediments (Bouchez et al., 2011; Grigolato et al.,

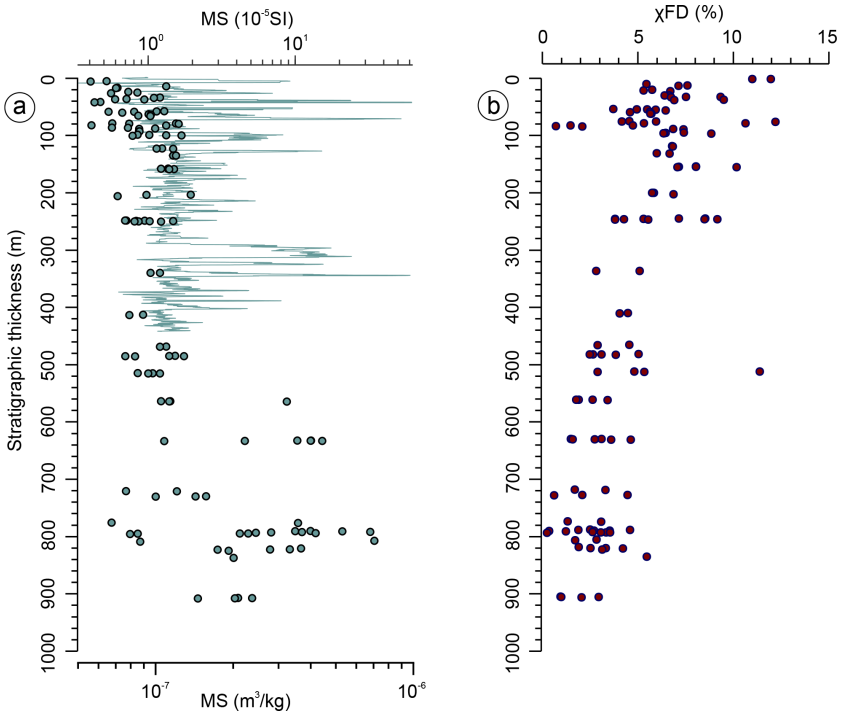

Figure 10. Magnetic susceptibility measurements and χFD% parameters. **(a)** Magnetic susceptibility against stratigraphic position. The continuous green line represents the MS data obtained on the whole core with a Geotek multi-sensor core logger (MSCL). These data were processed using a moving window of 200 points. MS data achieved from oriented samples are represented by green dots. **(b)** Variations in χFD% parameters are shown throughout the sedimentary succession, highlighting differences and trends.

2025). Interestingly, the average ln(Fe / K) value (0.56) of our record is similar to the average value of modern suspended sediments of the Solimões (1.02) and Madeira (0.71) rivers (Grigolato et al., 2025). Completing the major elemental analyses for the whole drilled section, as well as performing other types of analyses (e.g., grain size), is necessary to support in-depth interpretations.

XRD analysis of all samples yielded average contents of 45.7 % ± 27.9 (2σ) for quartz, 29.5 ± 29.3 for clay minerals plus mica, 20.5 ± 14.2 for feldspar, 3.9 ± 12.4 for carbonates, and 0.4 ± 1.3 for other minerals. The high standard deviation values reflect the compositional variability between lithotypes, mainly represented by sandstones and mudstones. Sandstones average 55.1 ± 13.3 for quartz, followed by feldspar at 22.2 ± 14.7, clay minerals plus mica at 20.5 ± 15.6, carbonates at 1.8 ± 4.8, and other phases at 0.4 ± 1.6. The high feldspar content of the sandstones indicates low mineralogical maturity, consistent with the occurrence of arkosic composition, whereas the elevated clay mineral proportion may be related to in situ feldspar alteration. Mudstones average 42.4 ± 24.6 for clay minerals plus mica, 32.3 ± 19.9 for quartz, 18.1 ± 12.0 for feldspar, 6.8 ± 16.7 for carbonates, and 0.4 ± 0.5 for other minor phases. As expected, these fine-grained siliciclastic rocks have a higher clay mineral content (Tucker and Jones, 2023). The relatively high carbonate content may be linked to early diagenetic processes within the sediment.

4.7.2 Organic geochemistry

TOC concentrations ranged from below the analytical detection limit to a maximum of 15.58 % (med = 0.06 %), with the highest values observed between approximately 500 and 720 m depth. The generally low TOC values throughout much of the record suggest extensive post-depositional degradation under oxic conditions. Although clay-rich facies are typically more favorable for organic matter preservation due to their low permeability and protective matrix, no clear correlation was identified between TOC content and grain size in the analyzed sample set. This suggests that rapid sedimentation events, capable of rapidly burying organic material and isolating it from oxidative degradation, may have played a key role in enhancing TOC preservation in portions of the record. The $\delta^{13}C$ of samples with TOC contents exceeding 0.15 % ranged from −26.28 ‰ to −24.66 ‰, consistent with a dominant contribution from C_3 terrestrial vegetation in these intervals.

Concentrations of sedimentary hydrocarbons are high in two intervals of the core: ∼ 150–250 m and below 500 m. Outside these intervals, sediments have low hydrocarbon yields that are more degraded and/or mature, and less

amenable to environmental reconstruction. Sediments contain *n*-alkanes, *n*-alkanoic acids, PAHs, and macrofossils that allow aspects of plant producers and depositional environments to be detected. No substantial heating and alteration occur in situ; however, low temperature, oxic degradation, and diagenesis likely explain the low abundances of biomarkers in the core in general. Low concentrations of *n*-alkanes ($< 1\,\mu g\,gdw^{-1}$) combined with maturity/degradation in the majority of samples precludes compound-specific C or H isotope analysis. $\delta^{13}C$ measurements on higher concentration *n*-alkanoic acids ($< 5\,\mu g\,gdw^{-1}$) yielded values ranging from $-27.2\,‰$ to $-36.6\,‰$, also consistent with a C_3 terrestrial vegetation signal. PAHs are detectable and commonly include retene, often used to denote the presence of gymnosperms, which is surprising as gymnosperms are rarely detected in the pollen assemblages; thus, other possible producers or diagenetic pathways appear likely.

4.7.3 Methane and carbon dioxide biogeochemistry

Preliminary results from the incubation experiments of sediment samples collected at 140.82 and 502.42 m depth show that, after 22 d of incubation at 25 °C, no detectable methane (CH_4) production occurred. In contrast, both samples exhibited a progressive increase in CO_2 concentrations that could be related to microbial activity or chemical weathering of inorganic carbon in the samples. The accumulation of CO_2 without concomitant CH_4 production suggests that processes other than methanogenesis are currently dominant, but it is still early to draw any conclusions as similar incubations using old subsurface sediment had a lag-phase longer than 30 d before CH_4 production started (Harris et al., 2008). In addition, substrate limitations, or competitive inhibition by alternative microbial processes, such as sulfate or iron reduction, could also limit or delay the production. These results highlight the importance of extending the incubation time beyond the initial 22 d to determine whether methane production will eventually occur once favorable redox conditions are established or labile substrates are consumed. Isotopic analysis of ^{13}C in CO_2 and eventually CH_4 at the end of the incubation period will help us to understand the pathways of production of these gases. Incubation experiments will help to determine if the methane detected regularly during drilling is partially derived from an active microbial gas system, a product of an ancient inactive microbial gas system, or migrated from a deep burial thermogenic gas system.

4.8 Biota

4.8.1 Pollen

To date, 1852 palynomorph species have been identified. The abundance of grass pollen increases to 12 % on average in 131 to 154 m, whereas there is a short spike of abundant *Podocarpus* at around 244 m, which suggests colder/drier conditions than modern. There is reworking of Cretaceous material in the 486 to 585 m interval. Many of the dominant floristic elements of the Pebas system (Jaramillo et al., 2025) are rare in the core, suggesting that the flora of the core belongs to a post-Pebas ecosystem that has rarely been studied as its sediments are rarely preserved. Most of the floral diversity is dominated by angiosperms, with no evidence of marine or brackish conditions. There are samples with high levels of diversity (up to 183 taxa in a count of 745), many of them being rare (one or two individuals), similar to modern rainforests.

4.8.2 Phytoliths

The 330 processed samples, which capture all but the top 140 m of the core, have been checked for phytolith recovery. The vast majority of these (300, or 91 %) did not yield any biogenic silica, and most also did not contain volcanic ash and secondarily precipitated silica, two types of non-biogenic silica with specific gravities that overlap with that of biosilica. So far, only 29 samples (8.8 %) featured rare phytoliths or diatoms, sponge spicules, and chrysophyte cysts that were well preserved. Among the phytolith morphotypes present, we identified potential palm phytoliths (SPHEROID ECHINATE) and an armed trichome (diagnostic of certain dicotyledonous angiosperms; Piperno, 2006), as well as less diagnostic forms (ELONGATE ENTIRE, ELONGATE DENTATE, and BLOCKY), all of which were exceedingly rare (one or two grains per slide). These marginally productive samples derive from lithologies ranging from claystone to sandstone, pointing to no clear pattern of preferential preservation linked to lithology. Because of the rarity of biosilica particles, we cannot rule out contamination during sample collection or processing. The overall lack of biosilica and other light silica (opal-A and similar) suggests that the chemical environment in the Acre core was not conducive to silica preservation in general, for example, due to high pH or abundant organic material, both of which have shown to accelerate silica dissolution (e.g., Song et al., 2016).

4.8.3 Ostracods

In the upper portion of the drill core record (0–513 m), the ostracod record is extremely poor, likely due to the depositional environment, which primarily is represented by paleosols. An interval in the lower sections of the core (789.02–793.30 m) contains a small number of ostracods, with at least three species of the ostracod genus *Cyprideis* (Fig. 11). Although very preliminary, these taxa are similar to those that are characteristic of the Pebas fauna (Gross et al., 2014; Gross and Piller, 2020).

4.8.4 Macrofossils

Macrofossils of plants, crustaceans, and vertebrates were found in several stratigraphic layers during the description

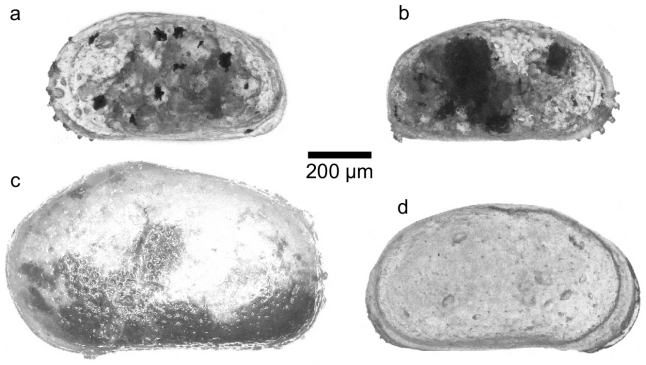

Figure 11. Ostracod taxa in the basal portions of the TADP-1A drill core.

and sampling of the Acre drill core. Preliminary identifications suggest that the fragments are reworked material derived primarily from sandy-conglomeratic layers and are associated with plant debris, coal associated with pyrite, rounded to sub-angular carbonate and cemented sandstone clasts, and mudclasts. These layers correspond to facies association FA1, and represent sharp erosional surfaces and/or co-sets of conglomerate and sandstone stacking. The only sample that differs from this relationship is 717.69 m, derived from mottled mudstone with peds, and rare and scarce iron hydroxide concretions. Preliminary identifications include crocodile teeth and a possible mammal bone, which ultimately could help to constrain sedimentation ages for the cores.

Fossils found in the following core sections are preliminarily identified as mammal rib and fish scales (882 m), an Actinopterygii fish tooth (497.95 m), fossil wood and a Potamotrygonidade stingray tooth (894.99 m), a possible mammal bone and coprolites (839.37 m), an Erythrinidae fish tooth (610.25 m), fish bone (842.09 m), a Eusuchia crocodylomorpha tooth (731.32 and 557.07 m), and a Tricholdactylidae crab pincer (717.69 m).

4.8.5 DNA microbiology

DNA extractions were consistently unsatisfactory: Qubit readings ranged from 0.08 to 0.2 ng μm^{-1}, no bands were observed on agarose gels, and all PCR attempts yielded negative results. Purification strategies, such as acetate or ethanol precipitation, QIAquick PCR purification kit, and magnetic beads also failed to significantly improve outcomes. These findings reflect challenges reported in other deep drilling projects, such the Collisional Orogeny in the Scandinavian Caledonides (COSC) project in Sweden. Westmeijer et al. (2024) reported similar difficulties when attempting to characterize microbial communities in deep rock samples. Despite applying six optimized extraction protocols and rigorous contamination control using fluorescent beads, the DNA extracted from core samples remained below detection limits, indicating extremely low biomass. Additionally, the Swedish study highlighted that, even after removing potential contaminants associated with drilling fluid, most sequences were affiliated with microorganisms known to be common reagent contaminants. The detection of native deep biosphere taxa, such as *Candidatus Desulforudis audaxviator*, occurred at levels below 0.1 % of total sequences, thus hindering any ecological interpretation. Given these challenges, the use of ancient DNA (aDNA) recovery strategies is suggested as a possible approach for future studies, involving specific reagents and techniques developed for low-biomass environments.

5 Outreach and geoconservation

The TADP incorporated outreach and geoconservation activities in the municipalities where drilling operations were conducted. These actions were part of a structured approach aiming to build trust, engage communities, and foster public appreciation for regional geodiversity and Earth sciences. In addition to these objectives, an inventory of 11 sites with geological significance in the Juruá River region was conducted and completed during the drilling phase (Fig. 12a). These geosites play a key role in conservation strategies and in the dissemination of scientific knowledge (Stewart, 2016).

Outreach efforts began in May 2023 prior to drilling operations, with on-site meetings held with local authorities to introduce the project and to clarify its scientific goals. This initial phase was followed by workshops for educators and public sector professionals, as well as school activities aimed at introducing geoscientific concepts specific to the Amazon region. These initiatives were complemented by lectures, community meetings, public talks, and local media engagement to ensure broad dissemination of the project's aims and methods (Fig. 12b).

The outreach strategy was based on three pillars:

i. Inventories focused on identifying geosites with high scientific, educational, and touristic potential (Brilha, 2018),

ii. Design thinking used to co-create solutions that were inclusive, locally relevant, and pedagogically effective (Gonsales, 2024; UNDP, 2017),

iii. Science communication and visual design (Ambrose and Harris, 2012; Williams, 2013), incorporating interpretive principles to produce clear and engaging messages for non-specialist audiences through printed and digital resources, following the principles of environmental interpretation (Tilden, 1957; Beck and Cable, 2002).

This approach resulted in the execution of 12 educational activities, including courses, workshops, lectures, field visits,

Figure 12. Outreach and geoconservation activities of TADP: **(a)** geosite Serra do Divisor, in the homonymous National Park, representative of the thrust tectonics related to the Andean uplift; **(b)** lecture to share TADP goals and geoscientific concepts for Rodrigues Alves students, teachers, and local administrators. Subsequent hands-on sessions were conducted to introduce participants to cores, rocks, minerals, and Amazon River sands; **(c)** themed postcards designed to highlight local geodiversity; **(d)** virtual tour mockup.

and hands-on sessions, reaching a total of 240 people. Participants included students of various ages, public school teachers, local administrators, and members of the general public. Teachers received educational resources, such as printed maps, books, and kits containing rocks, minerals, and sands, which now support ongoing classroom teaching.

The post-drilling phase marked the transition to the development of educational and outreach materials, co-created with local collaborators and researchers. These included printed products (folders, postcards, booklets), digital resources (educational videos, interactive visual content), and tactile tools (Fig. 12c). A virtual tour featuring 21 panoramic 360° aerial and ground-level images was also developed (Fig. 12d). This tour traces a geocultural itinerary across the region, from the Serra do Divisor, along the Moa and Juruá rivers, through the towns of Cruzeiro do Sul and Rodrigues Alves, and finally to the Croa River. Each location in the tour includes interactive hotspots that deliver interpretative content through pop-up windows and embedded videos.

6 Discussion

6.1 Paleoenvironments, paleovegetation, and paleoclimate

Throughout its entire extent, the Acre drill core (TADP-1A) contains alluvial sediments that were deposited in a large river system, including fluvial channels, bars, bar tops, and floodplain facies, with recurrent pedogenetic alteration of both fine-grained and sandy facies. Except for the uppermost ~ 12 m, all the lower sediments represent a single lithostratigraphic unit assigned to the Solimões Formation (Maia et al., 1977; Cunha, 2007). The feldspar-rich sands of the Solimões Formation, with low OSL sensitivity quartz, indicate an Andean provenance, whether directly from the Andes or reworked from older Andean deposits, and similar to sands transported by the modern Solimões and Madeira rivers (Sawakuchi et al., 2018). The sands from the upper 12 m are rich in quartz, with moderate to high OSL sensitivity, pointing to mixed Andean and lowland sources. The shift from feldspar to quartz-rich sands at ~ 12 m depth suggests a major change in sediment sources, possibly associated with the disconnection between the Andes and the Acre drainage systems, leading to the assembly of the modern watersheds

of the Juruá and Purus rivers with headwaters in the uplifted Acre Basin. The detrital zircon U-Pb ages, Nd and Sr isotopes, elemental ratios (Fe / K), and heavy mineral data also point to the dominance of Andean sources for the Solimões Formation sediments (12–923 m depth), with downcore variations suggesting changes in the sediment production and transport systems, possibly linked to climate and tectonic-induced changes in relief through time.

Only a small fraction of the pollen-bearing units has been analyzed for taxonomic composition, thus inferences about the vegetation are tentative. The analyzed sequences are commonly very diverse and have elements of both floodplain and terra firme (upland) forest. It is notable that the percentages of grasses, cycads, and conifers are consistently low; thus, there is no evidence of extensive savannah or conditions significantly drier than today. *Pediastrum* percentages are also low, which is consistent with the limited occurrence of lacustrine sedimentary sequences.

The presence of numerous paleosol horizons containing calcite concretions and, locally, gypsum crystals (in the lower stratigraphic levels) is distinctive, but it is not yet clear if the carbonate and sulfate are pedogenetic or eodiagenetic cements indicating a drier climate or if they are products of burial diagenesis. As of yet, none of the analyzed pollen samples suggests a climate much more arid or seasonal than today, which suggests that the carbonate and sulfate may not be syndepositional but instead may be the result of hydrothermal or mesodiagenetic processes. This is consistent with the observation of carbonate and sulfate veins within fractures or faults in regional outcrops, which indicate the migration of fluids from depth. The presence of ethane, propane, and butane (thermogenic hydrocarbons) (Martinez et al., 2025) also suggests that deeper diagenetic fluids migrated into the drilled units. However, additional geochemical and petrographic analyses are required to shed light on the origin of the authigenic calcite and gypsum. Diagenetic processes might also explain the general paucity of fossil phytoliths, diatoms, and other biosilica, which consist of extremely labile opal-A, in the core.

Cunha (2007) previously described a prevalence of fine-grained fluvio-lacustrine sediments in the upper part of the sedimentary sequence recovered in deep drill cores from the Acre Basin. While some earlier studies interpreted exposed Miocene deposits in the Acre Basin to have had local tidal influence (e.g., Räsänen et al., 1995), these strata were subsequently reinterpreted (Westaway, 2006; Latrubesse et al., 2007, 2010) as having been deposited in large fluvial systems. Latrubesse et al. (2010) concluded that the entire Late Miocene (9–6.5 Ma) sequence of the Acre Basin was deposited in fluvial depositional systems (comprising various facies, such as channels, floodplains, and floodplain lakes). Thus, the alluvial facies associations and paleosols found throughout the entire drilled succession were not unexpected.

6.2 Chronology

The target depth for drilling in the Acre Basin was 2000 m, which likely would have contained the entire Cenozoic sedimentary sequence. However, drilling was terminated at 923 m depth due to operational difficulties. Thus, the TADP-1A core only recovered a portion of the Solimões Formation and the overlying undifferentiated younger sediments in the upper 12 m. An Early to Middle Miocene age was previously attributed to the Solimões Formation in the Acre Basin (da Silva-Caminha et al., 2020), spanning several million years (23–11 Ma). According to Jaramillo et al. (2025), Pliocene sediments are not preserved in the Solimões Basin, where the Solimões Formation was defined, containing only Miocene sediments overlain by Pleistocene sediments of the Içá Formation.

The current age constraints on the TADP-1A core include quartz and feldspar luminescence geochronology, U-Pb detrital zircon measurements, and the pollen biostratigraphy. The uppermost ~ 12 m of the core sit above an erosional unconformity and are distinguished from feldspar-rich units below by mature sandy sediments with dominance of quartz. The age of this upper unit is uncertain, although the quartz OSL and feldspar $pIRIR_{290}$ ages suggest it is likely older than ~ 250 ka (Middle Pleistocene). Thus, luminescence age constraints indicate that the upper portion of the TADP-1A core is older than the Içá Formation, which covers the Solimões Formation in areas northwest of the Acre drill site (Pupim et al., 2019). The basal age of the drilled sequence is also somewhat uncertain. A sample at 863 m has a U-Pb zircon MDA estimate of 11.8 ± 0.4 Ma. U-Pb zircon ages yield a robust MDA estimate of 5.8 ± 0.21 Ma for a sample at 178 m depth, suggesting Pliocene sediments could occur in the upper portion of the TADP-1A core. An upward decrease in detrital zircon MDA ages suggests a time span from 12 to 6 Ma for the lower portion of the TADP-1A core (< 178 m depth), assuming that youngest zircon grains derive from active volcanism contemporary to sedimentation.

The assemblage of palynomorphs in the analyzed samples from the TADP-1A core differs from those from sites in other Cenozoic sequences of the general region, including Contamana in Peru (Antoine et al., 2016) and the Solimões Basin of northwestern Brazil (Jaramillo et al., 2025). These sequences extend through the Early to Middle Miocene and have short intervals that contain abundant marine palynomorphs. Both regions also show evidence of extensive and long-lived wetlands attributed to the Miocene Pebas Formation (Wesselingh et al., 2006) defined in northeastern Peru. In contrast, the TADP-1A drill core pollen stratigraphy does not contain marine palynomorphs, nor some of the dominant Middle Miocene floral elements at these other sites, such as *Mauritiidites* and *Grimsdalea*, suggesting that the Acre drill core is younger in age than the Contamana sediments or the Solimões Basin sequence examined by Jaramillo et al. (2025). The pollen assemblage suggests a latest Miocene

age (< 7 Ma) for the upper half of the drilled sections, which agrees with the MDA age of ∼ 6 Ma (maximum deposition age) at 178 m depth. Thus, the Solimões Formation in the TADP-1A core could represent sedimentation during the terminal phase of the Late Miocene or during the Pliocene. The deposition and preservation of Pliocene sediments in the TADP-1A drill site challenges the proposed timing or regional extent of uplift related to the Fitzcarrald Arch (Espurt et al., 2010). Ongoing work, including palynological, cosmogenic nuclides (Be-10 and Al-26), (U–Th) / He, U / Pb, feldspar and quartz luminescence, and paleomagnetism analyses, will provide more precise geochronological constraints.

7 Concluding remarks

Clarifying the time span encompassed by the TADP-1A core is needed to resolve major scientific questions about the history of Amazonia and its biodiversity. The emerging results suggest that the TADP-1A sequence, while not extending through the Cenozoic as hoped, may span later intervals of time (Late Miocene and Pliocene) not currently represented by existing records of the history of vegetation, climate, and the physical landscape. Thus, we have the promise of generating a novel high-resolution view of an important interval that is under-represented elsewhere in the western Amazon and central Andes. Most extant Amazonian species appeared during the Late Miocene and Pliocene (Rull, 2011). The uplift of some portions of the Andes also accelerated during this time, promoting marked landscape change linked to the reorganization of drainages and the filling of Subandean basins (Horton, 2018). Finally, the Late Miocene and Pliocene CO_2 levels are similar to the values for the year 2025 (Cenozoic CO_2 Proxy Integration Project (CENCO-PIP) Consortium, 2023) and what we will experience over the coming decades. Thus, the Late Miocene and Pliocene are key intervals for understanding the assembly of Amazon biodiversity and its response to landscape changes induced by Andean tectonics and global climate change. In addition, the TADP-2A core from the Marajó Basin in eastern Amazonia also likely comprises Late Miocene and Pliocene sediments. Together, these sequences have great potential to improve our understanding of the history of the Amazon vegetation, climate, and physical landscape across the entire basin during the late Cenozoic.

Data availability. All on-site core and section metadata, preliminary lithological descriptions, and all on-site sample metadata were recorded in ICDP's mobile Drilling Information System (mDIS). In addition, all data generated during the initial core processing at the CSD facility, including sample metadata, multi-sensor core logging data, core images, and complete lithologic descriptions, are archived according to standard data management systems at the CSD facility and are shared internally via a project-specific online collaboration space established in the Open Science Framework (OSF). TADP operates in accordance with the CSD facility and US National Science Foundation (NSF) rules regarding data availability, including a 2-year access moratorium period following the generation of samples or data. Pollen images and counts are part of the Smithsonian long-term curated collection (Jaramillo and Rueda, 2025).

Author contributions. Baker, Fritz, and Silva designed the TADP and wrote the initial ICDP grant. Baker, Fritz, Noren, Sawakuchi, and Silva oversaw the planning and execution of the drilling. Bezerra served as the Acre on-site project manager, with Sergio as the company man. Fritz oversaw the organization and drafting of this article and wrote major portions; and Sawakuchi, Noren, Baker, Almeida, Janikian, Jaramillo, Barbosa, Bertassoli, Bezerra, Blankenship, Chiessi, Feakins, Garcia, Gautheron, Grivna, Hartmann, Kunkel, Marconato, Martinez, Marulanda, Mazoca, Mui, Negri, Parra, Piller, Pupim, Salgado, Silva, So, Souza, Stiles, Strömberg, Wahnfried, and West contributed to writing and editing of portions the article and/or to drafting the figures. All authors contributed to fieldwork, core sampling, and/or laboratory analyses of the drill cores.

Competing interests. The contact author has declared that none of the authors has any competing interests.

Disclaimer. Publisher's note: Copernicus Publications remains neutral with regard to jurisdictional claims made in the text, published maps, institutional affiliations, or any other geographical representation in this paper. The authors bear the ultimate responsibility for providing appropriate place names. Views expressed in the text are those of the authors and do not necessarily reflect the views of the publisher.

Acknowledgements. We thank GEOSOL management (Thiago Sillman Borges, Dalmo Pereira, Mario Santos); GEOSOL lead drillers (Sebastian, Joacir, Everaldo); the landowner (Tárcito de Oliveira Batista); Uli Harms and Jochem Kueck of ICDP OSG; Leandro Domingos Luz of the CSD facility; Christovam Sanches and Luiz Ferradans of GEOFLUX for their assistance in planning, mobilizing, and executing the drilling of Acre; and M. Balvay and S. Campillo for their technical support in generating the (U–Th) / He data.

Financial support. Drilling and project development were supported by an ICDP award to PAB, SCF, CGS, and AM (ICDP-2017/01); NSF Integrated Earth Systems awards to PAB (1812681), SCF (1812857), and AN (1812752); NSF Instrumentation and Facilities awards to AN (1338322, 1951112); FAPESP awards to AOS (2018/23899-2, 2023/00448-3); and STRI funding to CJ (Smithsonian Tropical Research Institute, the Anders Foundation, 1923 Fund, Gregory D. and Jennifer Walston Johnson, the McLain Foundation, Maximilian of Liechtenstein, Robert Rooney, the Smithsonian Women's Committee, the Rubinoff Big Bet Endowment, and the SI Life on a Sustainable Planet Pathfinder).

These grants also provided research support, as did grants to CMC (FAPESP 2018/15123-4, 2019/24349-9, 2024/00949-5), KF (NSF-1812541), GH (FAPESP 2023/04179-7), CH and GB (Pieter Langerhuizen Lambertuszoon-Fonds 2022), CH (Bass Senior Visiting Fellowship), WEP (Austrian Academy of Sciences), FNP (FAPESP 2022/03007-5), HX (Chinese Scholarship Council No. 202306380061), and BZ (FWF 10.55776/P35815).

Review statement. This paper was edited by Hendrik Vogel and reviewed by Jonathan Obrist-Farner and one anonymous referee.

References

Allan, C., Burel, J.-M., Moore, J., Blackburn, C., Linkert, M., Loynton, S., MacDonald, D., Moore, W. J., Neves, C., Patterson, A., Porter, M., Tarkowska, A., Loranger, B., Avondo, J., Lagerstedt, I., Lianas, L., Leo, S., Hands, K., Hay, R. T., Patwardhan, A., Best, C., Kleywegt, Gerard J., Zanetti, G., and Swedlow, J. R.: OMERO: flexible, model-driven data management for experimental biology, Nat. Methods, 9, 245–253, https://doi.org/10.1038/nmeth.1896, 2012.

Allègre, C. J., Dupré, B., Négrel, P., and Gaillardet, J.: Sr-Nd-Pb isotope systematics in Amazon and Congo River systems: constraints about erosion processes, Chem. Geol., 131, 93–112, https://doi.org/10.1016/0009-2541(96)00028-9, 1996.

Almeida, R. P., Althaus, C. E., Janikian L., Gomes, P. V. O, Figueiredo, F. T., Sawakuchi, A. O., Freitas, B. T., and Silva, L. H. G.: Reappraisal of the Cretaceous and Paleogene paleogeography of eastern Amazonia based on systematic paleocurrent measurements, Cretaceous Res., 163, 105948, https://doi.org/10.1016/j.cretres.2024.105948, 2024.

Ambrose, G. and Harris, P.: Fundamentos de Design Criativo, Bookman Editora, 191 pp., ISBN 9788540701274, 2012.

Andò, S.: Gravimetric separation of heavy minerals in sediments and rocks, Minerals, 10, 273, https://doi.org/10.3390/min10030273, 2020.

Antoine, P.-O., Abello, M. A., Adnet, S., Sierra, A. J. A., Baby, P., Billet, G., Boivin, M., Calderon, Y., Candela, A. Chabain, J., Corfu, F., Croft, D. A., Ganerød, M., Jaramillo, C., Klaus, S., Marivaux, L., Navarrete, R. E., Orliac, M. J., Parra, F., Pérez, M. E., Pujos, F., Rage, J.-C., Ravel, A., Robinet, C., Roddaz, M., Tejada-Lara, J. V., Vélez-Juarbe, J., Wesselingh, F. P., and Salas-Gismondi, R.: A 60-million-year Cenozoic history of western Amazonian ecosystems in Contamana, eastern Peru, Gondwana Res., 31, 30–59, https://doi.org/10.1016/j.gr.2015.11.001, 2016.

Baker, P. A., Fritz, S. C., Silva, C. G., Rigsby, C. A., Absy, M. L., Almeida, R. P., Caputo, M., Chiessi, C. M., Cruz, F. W., Dick, C. W., Feakins, S. J., Figueiredo, J., Freeman, K. H., Hoorn, C., Jaramillo, C., Kern, A. K., Latrubesse, E. M., Ledru, M. P., Marzoli, A., Myrbo, A., Noren, A., Piller, W. E., Ramos, M. I. F., Ribas, C. C., Trnadade, R., West, A. J., Wahnfried, I., and Willard, D. A.: Trans-Amazon Drilling Project (TADP): origins and evolution of the forests, climate, and hydrology of the South American tropics, Sci. Dril., 20, 41–49, https://doi.org/10.5194/sd-20-41-2015, 2015.

Beck, L. and Cable, T. T.: Interpretation for the 21st century: Fifteen guiding principles for interpreting nature, ISBN 1571671331, 2002.

Bertassoli, D. J., Sawakuchi, A. O., Chiessi, C. M., Schefuss, E., Hartmann, G. A., Haggi, C., Cruz, F. W., Zabel, M., McGlue, M. M., Santos, R. A., and Pupim, F. N.: Spatiotemporal variations of riverine discharge within the Amazon Basin during the Late Holocene coincide with extratropical temperature anomalies, Geophys. Res. Lett., 46, 9013–9022, https://doi.org/10.1029/2019GL082936, 2019.

Bicudo, T. C., Sacek, V., Almeida, R. P, Bates, J. M., and Ribas, C. C.: Andean tectonics and mantle dynamics as a pervasive influence on Amazonian ecosystem, Sci. Rep., 9, 16879, https://doi.org/10.1038/s41598-019-53465-y, 2019.

Bicudo, T. C., Sacek, V., and Almeida, R. P.: Reappraisal of the relative importance of dynamic topography and Andean orogeny on Amazon landscape evolution, Earth Planet. Sc. Lett., 546, 116423, https://doi.org/10.1016/j.epsl.2020.116423, 2020.

Bishop, B. T., Beck, S. L., Zandt, G., Wagner, L., Long, M., Antonijevic, S. K., Kumar, A., and Tavera, H.: Causes and consequences of flat-slab subduction in southern Peru, Geosphere, 13, 1392–1407, https://doi.org/10.1130/GES01440.1, 2017.

Bouchez, J., Gaillardet, J., France-Lanord, C., Maurice, L., and Dutra-Maia, P.: Grain size control of river suspended sediment geochemistry: clues from Amazon River depth profiles, Geochem. Geophy. Geosy., 12, Q03008, https://doi.org/10.1029/2010GC003380, 2011.

Brilha, J.: Geoheritage: inventories and evaluation, Geoheritage, 4, 69–86, 2018.

Buylaert, J.-P., Jain, M., Murray, A. S., Thompson, K. J., Thiel, C., and Sohbati, R.: A robust feldspar luminescence dating method for middle and late Pleistocene sediments, Boreas, 41, 435–451, https://doi.org/10.1111/j.1502-3885.2012.00248.x, 2012.

Caputo, M. V. and Soares, E. A.: Eustatic and tectonic change effects in the reversion of the transcontinental Amazon River drainage system, Braz. J. Geol., 46, 301–328, https://doi.org/10.1590/2317-4889201620160066, 2016.

Cenozoic CO_2 Proxy Integration Project (CENCO-PIP) Consortium: Toward a Cenozoic history of atmospheric CO_2, Science, 382, eadi5177, https://doi.org/10.1126/science.adi5177, 2023.

Cheary, R. W. and Coelho, A.: A fundamental parameters approach to X-ray line-profile fitting, Appl. Crystallogr., 25, 109–121, https://doi.org/10.1107/S0021889891010804, 1992.

Cheng, H., Sinha, A., Cruz, F. W., Wang, X., Edwards, R. L., D'Horta, F. M., Ribas, C. C., Vuille, M., Stott, L. D., and Auler, A. S.: Climate change patterns in Amazonia and biodiversity, Nat. Commun., 4, 1411, https://doi.org/10.1038/ncomms2415, 2013.

Cordani, U. G., Ramos, V. A., Fraga, L. M., Cegarra, M., Delgado, I., Souza, K. G., Gomes, F. E. M., and Schobbenhaus, C.: Tectonic map of South America: scale 1 : 5 000 000, Commission for the Geological Map of the World, Paris, France, https://doi.org/10.14682/2016TEMSA, 2016.

CPRM (Serviço Geológico do Brasil): Mapa cronoestratigráfico simplificado do Brasil, scale 1:5,000,000, https://rigeo.sgb.gov.br/handle/doc/17619 (last access: 8 June 2026), 2015.

Crifò, C. and Strömberg, C. A.: Spatial patterns of soil phytoliths in a wet vs. dry Neotropical forest: implica-

tions for paleoecology, Palaeogr. Palaeocl. Palaeoec., 562, https://doi.org/10.1016/j.palaeo.2020.110100, 2021.

Cunha, P. R. C.: Bacia do Acre, Boletim de Geociências da Petrobras, 15, 207–215, 2007.

da Silva-Caminha, S. A. F., D'Apolito, C., Jaramillo, C., Espinosa, B. S., and Rueda, M.: Palynostratigraphy of the Ramon and Solimões formations in the Acre Basin, Brazil, J. South Am. Earth Sci., 103, 102720, https://doi.org/10.1016/j.jsames.2020.102720, 2020.

Dearing, J. A., Livingstone, I., and Zhou, L. P.: A late Quaternary magnetic record of Tunisian loess and its climatic significance, Geophys. Res. Lett., 23, 189–192, https://doi.org/10.1029/95GL03132, 1996.

DePaolo, D. J.: Trace element and isotopic effects of combined wallrock assimilation and fractional crystallization, Earth Planet. Sc. Lett., 53, 189–202, https://doi.org/10.1016/0012-821X(81)90153-9, 1981.

Dickau, R., Whitney, B. S., Iriarte, J., Mayle, F. E. , Soto, J. D., Metcalfe, P., Street-Perrott, F. A., Loader, N. J., Ficken, K. J., and Killeen, T. J.: Differentiation of neotropical ecosystems by modern soil phytolith assemblages and its implications for palaeoenvironmental and archaeological reconstructions, Rev. Palaeobot. Palyno., 193, 15–37, https://doi.org/10.1016/j.revpalbo.2013.01.004, 2013.

Erzinger, J., Wiersberg, T., and Zimmer, M.: Real-time mud gas logging and sampling during drilling, Geofluids, 6, 225–233, https://doi.org/10.1111/j.1468-8123.2006.00152.x, 2006.

Espinoza, J. C., Ronchail, J., Guyot, J. L., Cochonneau, G., Naziano, F., Lavado, W., Olivera, E., Pombosa, R., and Vauchel, P.: Spatio-temporal rainfall variability in the Amazon Basin countries (Brazil, Peru, Bolivia, Colombia, and Ecuador), Int. J. Climatol., 29, 1574–1594, https://doi.org/10.1002/joc.1791, 2009.

Espurt, N., Baby, P., Brusset, S., Roddaz, M., Hermoza, W., Regard, V., Antoine, P.-O., Salas-Gismondi, P. R., and Bolaños, R.: How does the Nazca Ridge subduction influence the modern Amazonian foreland basin?, Geology, 35, 515–518, https://doi.org/10.1130/g23237A.1, 2007.

Espurt, N., Baby, P., Brusset, S., Roddaz, M., Hermoza, H., and Barbarian, J.: The Nazca Ridge and uplift of the Fitzcarrald Arch: implications for regional geology in northern South America, in: Amazonia, Landscape and Species Evolution (1st edition), edited by: Hoorn, C. and Wesselingh, F. P., Blackwell Publishing, ISBN 978-1-4051-8113-6, 2010.

Etiope, G. and Schwietzke, S.: Global geological methane emissions: An update of top-down and bottom-up estimates, Elem. Sci. Anth., 7, 47, https://doi.org/10.1525/elementa.383, 2019.

Expedition 337 Scientists: Methods, edited by: Inagaki, F., Hinrichs, K.-U., Kubo, Y., and the Expedition 337 Scientists, Proc. IODP, 337, Integrated Ocean Drilling Program Management International, Inc., Tokyo, https://doi.org/10.2204/iodp.proc.337.102.2013, 2013.

Figueiredo, J., Hoorn, C., van der Ven, P., and Soares, E.: Late Miocene onset of the Amazon River and the Amazon deep-sea fan: Evidence from the Foz do Amazonas Basin, Geology, 37, 619–622, https://doi.org/10.1130/G30633C.1, 2009.

Frailey, C. D., Lavina, E. L. , Rancy, A., and de Souza-Filho, J. P.: A proposed Pleistocene/Holocene lake in the Amazon basin and its significance to Amazonian geology and biogeography, Acta Amazon., 18, 119–143, https://doi.org/10.1590/1809-43921988183143, 1988.

Galehouse, J. S.: Point counting, in: Procedures in sedimentary petrology, edited by: Carver, R. E., Wiley, New York, 385–407, ISBN: 9780471138556, 1971.

Gat, J. R. and Matsui, E.: Atmospheric water balance in the Amazon basin: an isotopic evapotranspiration model, J. Geophys. Res. Atm., 96, 13179–13188, https://doi.org/10.1029/91JD00054, 1991.

Gautheron, C., Espurt, N., Barbarand, J., Roddaz, M., Baby, P., Brusset, S., Tassan-got, L., and Douville, E.: Direct dating of thick- and thin-skin thrusts in the Peruvian Subandean zone through apatite (U–Th) / He and fission track thermochronometry, Basin Res., 25, 419–435, https://doi.org/10.1111/bre.12012, 2013.

Gautheron, C., Pinna-Jamme, R., Derycke, A., Ahadi, F., Sanchez, C., Haurine, F., Monvoisin, G., Barbosa, D., Delpech, G., Maltese, J., Sarda, P., and Tassan-Got, L.: Technical note: Analytical protocols and performance for apatite and zircon (U–Th) / He analysis on quadrupole and magnetic sector mass spectrometer systems between 2007 and 2020, Geochronology, 3, 351–370, https://doi.org/10.5194/gchron-3-351-2021, 2021.

Gautheron, C., Sawakuchi, A. O., Santos Albuquerque, M. F., Cabriolu, C., Parra, M., Ribas, C. C., Pupim, F. N., Schwartz, S., Kern, A. K., Gómez, S., Almeida, R. P., Horbe, A. M. C., Haurine, F., Miska, J. S., Nouet, J., Findling, N., Riffel, S. B., and Pinna-Jamme, R.: Cenozoic weathering of fluvial terraces and emergence of biogeographic boundaries in Central Amazonia, Global Planet. Change, 212, 103815, https://doi.org/10.1016/j.gloplacha.2022.103815, 2022.

Gehrels, G. E., Valencia, V. A., and Ruiz, J.: Enhanced precision, accuracy, efficiency, and spatial resolution of U-Pb ages by laser ablation-multicollector-inductively coupled plasma-mass spectrometry, Geochem., Geophy., Geosy., 9, https://doi.org/10.1029/2007GC001805, 2008.

Gonsales, P.: Design Thinking para Educadores, Instituto Educadigital, 76 pp., https://www.academia.edu/31989372/Design_Thinking_para_Educadores (last access: 5 June 2026), 2024.

Govin, A., Holzwarth, U., Heslop, D., Keeling, L. F., Zabel, M., Mulitza, S., Collins, J. A., and Chiessi, C. M.: Distribution of major elements in Atlantic surface sediments (36 degrees N-49 degrees S): Imprint of terrigenous input and continental weathering, Geochem. Geophy. Geosy., 13, Q01013, https://doi.org/10.1029/2011GC003785, 2012.

Grigolato, J., Chiessi, C. M., Bertassoli, D. J., Campos, M. C., Shimizu, M. H., Magalhães, R. H., Nace, T., Sawakuchi, A. O., Wahnfried, I. D., Neri, R., Cunha, A. C., Silva, C. G., Baker, P. A., Govin, A., and Zabel, M.: Past Amazon precipitation under different Atlantic Meridional Overturning Circulation and sea surface temperature scenarios of the last deglaciation, Quaternary Sci. Rev., 362, 109425, https://doi.org/10.1016/j.quascirev.2025.109425, 2025.

Gross, M. and Piller, W. E.: Saline waters in Miocene western Amazonia – an alternative view, Front. Earth Sci., 8, 116, https://doi.org/10.3389/feart.2020.00116, 2020.

Gross, M., Ramos, M. I., Caporaletti, M., and Piller, W. E.: Ostracods (Crustacea) and their palaeoenvironmental implication for the Solimões Formation (Late Miocene; Western

Amazonia/Brazil), J. South Am. Earth Sci., 42, 216–241, https://doi.org/10.1016/j.jsames.2012.10.002, 2013.

Gross, M., Ramos, M. I. F., and Piller, W. E.: On the Miocene *Cyprideis* species flock (Ostracoda; Crustacea) of Western Amazonia (Solimões Formation): Refining taxonomy on species level, Zootaxa, 3899, 1–69, https://doi.org/10.11646/zootaxa.3899.1.1, 2014.

Guérin, G., Mercier, N., and Adamiec, G: Dose-rate conversion factors: update, Ancient TL, 29, 5–8, 2011.

Harris, S. H., Smith, R. L., and Barker, C. E.: Microbial and chemical factors influencing methane production in laboratory incubations of low-rank subsurface coals, Int. J. Coal Geol., 76(1-2), 46-51, https://doi.org/10.1016/j.coal.2008.05.019, 2008

Hoorn, C., Boschman, L. M., Kukla, T., Sciumbata, M., and Val, P.: The Miocene wetland of western Amazonia and its role in Neotropical biogeography, Bot. J. Linn. Soc., 199, 25–35, https://doi.org/10.1093/botlinnean/boab098, 2022.

Hoorn, C., Lohmann, L. G., Boschman, L. M., and Condamine, F. L.: Neogene history of the Amazonian flora: a perspective based on geological, palynological, and molecular phylogenetic data, Annu. Rev. Earth Pl. Sc., 51, 419–446, https://doi.org/10.1146/annurev-earth-081522-090454, 2023.

Höppner, N., Lucassen, F., Chiessi, C. M., Sawakuchi, A. O., and Kasemann, S. A.: Holocene provenance shift of suspended particulate matter in the Amazon River basin, Quaternary Sci. Rev., 190, 66–80, https://doi.org/10.1016/j.quascirev.2018.04.021, 2018.

Horbe, A. M. C., Roddaz, M., Gomes, L. B., Castro, R. T., Dantas, E. L., and do Carmo, D. A.: Provenance of the Neogene sediments from the Solimões Formation (Solimões and Acre Basins), Brazil, J. S. Am. Earth Sci., 93, 232–241, https://doi.org/10.1016/j.jsames.2019.05.004, 2019.

Horton, B. K.: Sedimentary record of Andean mountain building, Earth Sci. Rev., 178, 279–309, https://doi.org/10.1016/j.earscirev.2017.11.025, 2018.

Jacobsen, S. B. and Wasserburg, G. J.: Sm-Nd isotopic evolution of chondrites, Earth Planet. Sc. Lett., 50, 139–155, https://doi.org/10.1016/0012-821X(80)90125-9, 1980.

Jaramillo, C. and Rueda, M.: A morphological electronic database of Cretaceous-tertiary fossil pollen and spores from Northern South America, Panama, Smithsonian Tropical Research Institute, https://biogeodb.stri.si.edu/jaramillosdb/web/morphological/m-index (last access: 5 June 2026), 2025.

Jaramillo, C., Romero, I., D'Apolito, C., Bayona, G., Duarte, E., Louwye, S., Escobar, J., Luque, J., Carrillo-Briceno, J. D., Zapata, V., Mora, A., Schouten, S., Zavada, M., Harrington, G., Ortiz, J., and Wesselingh, F.: Miocene flooding events of Western Amazonia, Sci. Adv., 3, e1601693, https://doi.org/10.1126/sciadv.1601693, 2017.

Jaramillo, C. A., D'Apolito, C., Silva-Caminha, S. A. F., and Caballero-Rodriguez, D.: A palynological zonation for the Neogene of the Solimões /Amazon Basin, northwestern Amazonia, Palynology, https://doi.org/10.1080/01916122.2024.2413153, 2025.

Karp, A. T., Andrae, J. W., McInerney, F. A., Polissar, P. J., and Freeman, K. H.: Soil carbon loss and weak fire feedbacks during Pliocene C4 grassland expansion in Australia, Geophys. Res. Lett., 48, e2020GL090964, https://doi.org/10.1029/2020GL090964, 2021.

Kern, A. K., Gross, M., Galeazzi, C. P., Pupim, F. N., Sawakuchi, A. O., Cheng, R. P., Piller, W. E., Kuhlmann, G. C., and Basei, M. A. S.: Re-investigating Miocene age control and paleoenvironmental reconstructions in western Amazonia (northwestern Solimões Basin, Brazil), Palaeogr. Palaeocl. Palaeoec., 545, 109652, https://doi.org/10.1016/j.palaeo.2020.109652, 2020.

Kistler, L.: Ancient DNA extraction from plants, in: Ancient DNA. Methods in Molecular Biology, edited by: Shapiro, B. and Hofreiter, M., 840, 71–79, https://doi.org/10.1007/978-1-61779-516-9, 2011.

Kraft, L., Campos, M. C., Nascimento, R. A., Dias, B. B., Crivellari, S., Kochhann, M. V. L., Bertassoli, D. J., Venancio, I. M., Santos, T. P., Baker, P. A., Silva, C. G., and Chiessi, C. M.: AMOC-forced southward migration of the ITCZ under a warm climate background, Palaeogr. Palaeocl. Palaeoec., 661, 112705, https://doi.org/10.1016/j.palaeo.2024.112705, 2025.

Latrubesse, E., Silva, S. F., Cozzuol, M., and Absy, M. L.: Late Miocene continental sedimentation in the southwestern Amazonia and its regional significance: Biotic and geological evidence, J. S. Am. Earth Sci., 23, 61–80, https://doi.org/10.1016/j.jsames.2006.09.021, 2007.

Latrubesse, E. M., Cozzuol, M., Silane, A. F., Rigsby, C. A., Absy, M., and Jaramillo, C.: The Late Miocene paleogeography of the Amazon Basin and the evolution of the Amazon River system, Earth Sci. Rev., 99, 99–124, https://doi.org/10.1016/j.earscirev.2010.02.005, 2010.

Mahan, S. A., Rittenour, T. M., Nelson, M. S., Ataee, N., Brown, N., DeWitt, R., and Thomsen, K.: Guide for interpreting and reporting luminescence dating results, GSA Bull., 135, 1480–1502, https://doi.org/10.1130/B36404.1, 2023.

Maia, R. G., Godoy, H. K., Yamaguti, H. S., Moura, P. A., Costa, F. S., Holanda, M. A., and Costa, J.: Projeto de carvão no Alto Solimões. Relatório Final, CPRM-DNPM, 137 pp., https://rigeo.sgb.gov.br/handle/doc/9392 (last access: 5 June 2026), 1977.

Martinelli, L. A., Victoria, R. L., Sternberg, L. S. L., Ribeiro, A., and Moreira, M. Z.: Using stable isotopes to determine sources of evaporated water to the atmosphere in the Amazon basin, J. Hydrol., 183, 191–204, https://doi.org/10.1016/0022-1694(95)02974-5, 1996.

Martinez, A. E. J, Sawakuchi, A. O., Bertassoli, D. J., Wiersberg, T., Tsai, S. M., Araújo, K. R., Tamura, L. N., Barbosa, M. B., Bicudo, T. C., de Brito, A. P., Wahnfried, I. D., Bezerra, I. S., Noren, A., Silva, C. G., Fritz, S. C., and Baker, P.: Subsurface gaseous hydrocarbons and carbon dioxide recorded during the Trans-Amazon Drilling Project (TADP) in the Acre Basin, western Amazon, Geofluids, https://doi.org/10.1155/gfl/6658750, 2025

Morcote-Ríos, G., Giraldo-Cañas, D., and Raz, L.: Phytoliths of Amazonian grasses: diversity and applications, Cinchonia 20, 18–58, 2025.

Murray, A. S. and Wintle, A. G.: The single aliquot regenerative dose protocol: potential for improvements in reliability, Radiat. Meas., 37, 377–381, https://doi.org/10.1016/S1350-4487(03)00053-2, 2003.

NASA JPL: NASADEM Merged DEM Global 1 arc second V00, OpenTopography, https://doi.org/10.5069/G93T9FD9, 2021.

Nascimento, D. R., Sawakuchi, A. O., Guedes, C. C. F., Giannini, P. C. F., Grohmann, C. H., and Ferreira, M. P.: Provenance of sands from the confluence of the Amazon and

Madeira rivers based on detrital heavy minerals and luminescence of quartz and feldspar, Sediment. Geol., 316, 1–12, https://doi.org/10.1016/j.sedgeo.2014.11.002, 2015.

Negri, F. R., Bocquentin-Villanueva, J., Ferigolo, J., and Antoine, P.-O.: A review of Tertiary mammal faunas and birds from western Amazonia, in: Amazonia: Landscape and Species Evolution, a Look into the Past, edited by: Hoorn, C. and Wesselingh, F. P., Wiley-Blackwell, 29–37, https://doi.org/10.1002/9781444306408, 2010.

Oliveira, R. S. and Vidotti, R. M.: The role of tectonic inheritance in the development of an Andean retroarc foreland basin system: The Acre Basin (NW Brazil), Mar. Petrol. Geol., 160, https://doi.org/10.1016/j.marpetgeo.2023.106645, 2024.

Peaple, M. D., Bhattacharya, T., Tierney, J. E., Knott, J. R., Lowenstein T. K., and Feakins, S. J.: Biomarker evidence for an MIS M2 glacial-pluvial in the Mojave Desert before warming and drying in the Late Pliocene, Paleoceanography and Paleoclimatology, 39, e2023PA004687, https://doi.org/10.1029/2023PA004687, 2024.

Pinto, L.: Traçage de l'érosion Cénozoïc des Andes Centrales à l'aide dela minéralogie et de la géochemie des sediments (Nord du Chili et Nord-Ouest de la Bolivie), PhD, University Paul Sabatier, http://www.theses.fr/2003TOU30034 (last access: 5 June 2026), 2003.

Piperno, D. R.: Phytoliths: A Comprehensive Guide for Archaeologists and Paleocologists, Altamira Press, ISBN 0759103852, 2006.

Pupim, F. N., Sawakuchi, A. O., Almeida, R. P., Ribas, C. C., Kern, A. K., Hartrmann, G. A., Chiessi, C. M., Tamura, L. N., Mineli, T. D., Savian, J. F., Grohmann, C. H., Bertassoli, D. J., Stern, A. G., Cruz, F. W., and Cracraft, J.: Chronology of Terra Firme formation in Amazonian lowlands reveals a dynamic Quaternary landscape, Quaternary Sci. Rev., 210, 154–163, https://doi.org/10.1016/j.quascirev.2019.03.008, 2019.

Räsänen, M. E., Linna, A. M., Santos, J. C. R., and Negri, F. R.: Late Miocene tidal deposits in the Amazonian foreland basin, Science, 269, 386–390, https://doi.org/10.1126/science.269.5222.386, 1995.

Ribas, C. C., Aleixo, A., Nogueira, A. C. R., Miyaki, C. Y., and Cracraft, J.: Amazonia over the past three million years, P. Roy. Soc. Lond. B. Bio., 279, 681–689, https://doi.org/10.1098/rspb.2011.1120, 2012.

Roddaz, M., Viers, J., Brusset, S., Baby, P., and Hérail, G.: Sediment provenances and drainage evolution of the Neogene Amazonian foreland basin, Earth Planet. Sc. Lett., 239, 57–78, https://doi.org/10.1016/j.epsl.2005.08.007, 2005.

Rull, V.: Neotropical biodiversity: timing and potential drivers, Trends Ecol. Evol., 26, 508–513, https://doi.org/10.1016/j.tree.2011.05.011, 2011.

Sacek, V., Mutz, S. G., Bicudo, T. C., Almeida, R. P., and Ehlers, T. A.: The Amazon paleoenvironment resulted from geodynamic, climate, and sea-level interactions, Earth Planet. Sc. Lett., 605, 118033, https://doi.org/10.1016/j.epsl.2023.118033, 2023.

Sawakuchi, A. O., Jain, M., Mineli, T. D., Nogueira, L., Bertassoli, D. J., Häggi, C., Sawakuchi, H. O., Pupim, F. N., Grohmann, C. H., Chiessi, C. M., Zabel, M., Mulitza, S., Mazoca, C. E. M., and Cunha, D. F.: Luminescence of quartz and feldspar fingerprints provenance and correlates with the source area denudation in the Amazon River basin, Earth Planet. Sc. Lett., 492, 152–162, https://doi.org/10.1016/j.epsl.2018.04.006, 2018.

Sawakuchi, H. O., Bastviken, D., Enrich-Prast, A., Ward, N. D., Camargo, P. B., and Richey, J. E.: Low diffusive methane emissions from the main channel of a large Amazonian run-of-the-river reservoir attributed to high methane oxidation, Front. Environ. Sci., 9, 655455, https://doi.org/10.3389/fenvs.2021.655455, 2021.

Song, Z., Mcgrouther, K., and Wang, H.: Occurrence, turnover and carbon sequestration potential of phytoliths in terrestrial ecosystems, Earth Sci. Rev., 158, 19–30, https://doi.org/10.1016/j.earscirev.2016.04.007, 2016.

Stewart, I.: Sustainable geoscience, Nat. Geosci., 9, 262, https://doi.org/10.1038/ngeo2678, 2016.

Stiles, E., Gelfo, J. N., Raigemborn, M. S. , Kohn, M. J., Canares, B. A., Trayler, R. B., Ibañez-Mejía, M., Erra, G., Goin, F., and Strömberg, C. A. E.: Phytoliths reveal Paleocene-Eocene forest expansions preceded dryland vegetation in southern South America, Geol. Soc. Am. Bull. 138, https://doi.org/10.1130/B38275.1, 2025.

Stirling, D.: DNA extraction from fungi, yeast, and bacteria, in: PCR Protocols. Methods in Molecular Biology, edited by: Bartlett, J. M. S. and Stirling, D., 226, 53–54, ISBN 978-0896036420, 2003.

Strömberg, C. A. E.: The origin and spread of grass-dominated ecosystems during the Tertiary of North America and how it relates to the evolution of hypsodonty in equids, PhD, University of California, Berkeley, https://backend.production.deepblue-documents.lib.umich.edu/server/api/core/bitstreams/6cdfdbb5-4766-448a-9f8b-1998a5cc327f/content (last access: 5 June 2026), 2003.

Strömberg, C. A. E., Dunn, R. E., Crifò, C., and Harris, E. B.: Phytoliths in paleoecology: Analytical considerations, current use, and future directions, in: Methods in Paleoecology. Reconstructing Cenozoic terrestrial environments and ecological communities, edited by: Croft, D. A., Simpson, S., and Su, D. F., Vertebrate Paleobiology and Paleoanthropology Book Series, Springer Publishers, 233–285, https://doi.org/10.1007/978-3-319-94265-0_12, 2018.

Sun, S., Schefuß, E., Mulitza, S., Chiessi, C. M., Sawakuchi, A. O., Zabel, M., Baker, P. A., Hefter, J., and Mollenhauer, G.: Origin and processing of terrestrial organic carbon in the Amazon system: lignin phenols in river, shelf, and fan sediments, Biogeosciences, 14, 2495–2512, https://doi.org/10.5194/bg-14-2495-2017, 2017.

Sundell, K. E., Gehrels, G. E., and Pecha, M. E.: Rapid U-Pb geochronology by laser ablation multi-collector ICP-MS, Geostand. Geoanal. Res., 45, 37–57, https://doi.org/10.1111/ggr.12355, 2021.

Tassinari, C. C. G., Cordani, U. G., Nutman, A. P., Schmus, W. R. V, Bettencourt, J. S., and Taylor, P. N.: Geochronological systematics on basement rocks from the Río Negro-Juruena Province (Amazonian Craton) and tectonic implications, Int. Geol. Rev., 38, 161–175, https://doi.org/10.1080/00206819709465329, 1996.

Tassinari, C. C. G., Bettencourt, J. S., Geraldes, M. C., Macambira, M. J. B., and Lafon, J. M.: The Amazonian craton, in: Tectonic Evolution of South America, The 31st International Geological Congress, Rio de Janeiro, Brazil, edited by: Cordani, U. G., Mi-

lani, E. J., Thomaz Filho, A., and Campos, D. A., 41–95, ISBN 8590148211, 2000.

ter Steege, H.: Hyperdominance in the Amazonian tree flora, Science 342, 12430921–12430929, https://doi.org/10.1126/science.1243092, 2013.

Tilden, F.: Interpreting Our Heritage, The University of North Carolina Press, ISBN 9780807858677, 1957.

Traverse, A.: Paleopalynology, Second Edition, Springer, Dordrecht, 813 pp., https://doi.org/10.1007/978-1-4020-5610-9, 2007.

Tucker, M. E. and Jones, S. J.: Sedimentary petrology, John Wiley & Sons, ISBN: 978-1-118-78648-2, 2023.

UNDP: Design Thinking: A Guide for Prototyping and Testing Solutions for Sustainable Development Goals, United Nations Development Programme, 48 pp., https://bility.wdo.org/wp-content/uploads/2021/03/Design-Thinking-A-guide-for-prototyping (last access: 5 June 2026), 2017.

Vasquez, V. R. and Whiting, W. B.: Accounting for both random errors and systematic errors in uncertainty propagation analysis of computer models involving experimental measurements with Monte Carlo methods, Risk Anal., 25, 1669–1681, https://doi.org/10.1111/j.1539-6924.2005.00704.x, 2005.

Vermeesch, P.: Maximum depositional age estimation revisited, Geosci. Front., 12, 843–850, https://doi.org/10.1016/j.gsf.2020.08.008, 2021.

Viers, J., Roddaz, M., Filizola, N., Guyot, J. L., Sondag, F., Brunet, P., Zouiten, C., Boucayrand, C., Martin, F., and Boaventura, G. R.: Seasonal and provenance controls on Nd-Sr isotopic compositions of Amazon rivers suspended sediments and implications for Nd and Sr fluxes exported to the Atlantic Ocean, Earth Planet. Sc. Lett., 274, 511–523, https://doi.org/10.1016/j.epsl.2008.08.011, 2008.

Wanderley-Filho, J. R., Eiras, J. F., Cunha, P. R. C., and van der Ven, P. H: The Paleozoic Solimões and Amazonas basins and the Acre foreland basin of Brazil, in: Amazonia: Landscape and Species Evolution, a Look into the Past, edited by: Hoorn, C. and Wesselingh, F. P., Wiley-Blackwell, 29–37, https://doi.org/10.1002/9781444306408, 2010.

Webb, S. D.: Biological implications of the middle Miocene Amazon seaway, Science, 269, 361–362, https://doi.org/10.1126/science.269.5222.361, 1995.

Wesselingh, F. P., Räsänen, M. E., Irion, G., Vonhof, H. B., Kaandorp, R., Renema, W., Romero Pittman, L., and Gringas, M.: Lake Pebas: A palaeoecological reconstruction of a Miocene, long-lived lake complex in western Amazonia, Cainozoic Res., 1, 35–81, 2006.

Westaway, R.: Late Cenozoic sedimentary sequences in Acre state, southwestern Amazonia: fluvial or tidal? Deductions from the IGCP 449 fieldtrip, J. S. Am. Earth Sci., 21, 120–134, https://doi.org/10.1016/j.jsames.2005.08.004, 2006.

Westmeijer, G., Escudero, C., Bergin, C., Turner, S., Ståhle, M., Mehrshad, M., Leroy, P., Buck, M., López-Hernández, P., Kallmeyer, J., Amils, R., Bertilsson, S., and Dopson, M.: Continental scientific drilling and microbiology: (extremely) low biomass in bedrock of central Sweden, Biogeosciences, 21, 591–604, https://doi.org/10.5194/bg-21-591-2024, 2024.

Wiersberg, T., Pierdominici, S., Lorenz, H., Almqvist, B., Klonowska, I., and COSC Science Team: Identification of gas inflow zones in the COSC-1 borehole (Jämtland, central Sweden) by drilling mud gas monitoring, downhole geophysical logging, and drill core analysis, Appl. Geochem., 114, 104513, https://doi.org/10.1016/j.apgeochem.2019.104513, 2020.

Wilkinson, M., Dumontier, M., Aalbersberg, I., Appleton, G., Axton,. M, Baak, A., Blomberg, N., Boiten, J.-W., Da Silva Santos, L. B., Bourne, P. E., Bouwman, J., Brookes, A. J., Clark, T., Crosas, M., Dillo, I., Dumon, O., Edmunds, S., Evelo, C. T., Finkers, R., Gonzalez-Beltran, A., Gray, A. J. G., Groth, P., Goble, C., Grethe, J. S., Heringa, J., Hoen, P. A. C., Hooft, R., Kuhn, T., Kok, R., Kok, J., Lusher, S. J., Martone, M. E., Mons, A., Packer, A. L., Persson, B., Rocca-Serra, P., Roos, M., Van Schaik, R., Sansone, S.-A., Schultes, E., Sengstag, T., Slater, T., Strawn, G., Swertz, M. A., Thompson, M., Van Der Lei, J., Van Mulligen, E., Velterop, J., Waagmeester, A., Wittenburg, P., Wolstencroft, K., Zhao, J., and Mons, B.: The FAIR Guiding Principles for scientific data management and stewardship, Sci. Data, 3, 160018, https://doi.org/10.1038/sdata.2016.18, 2016.

Williams, R.: Design para quem não é designer: princípios de design e tipografia para iniciantes, Callis, 216 pp., ISBN 857416836X, 2013.

Zabel, M., Schneider, R. R., Wagner, T., Adegbie, A. T., De Vries, U., and Kolonic, S.: Late Quaternary climate changes in central Africa as inferred from terrigenous input to the Niger Fan, Quaternary Res., 56, 207–217, https://doi.org/10.1006/qres.2001.2261, 2001.

Zhang, Y. C., Chiessi, C. M., Mulitza, S., Zabel, M., Trindade, R. I. F., Hollanda, M., Dantas, E. L., Govin, A., Tiedemann, R., and Wefer, G.: Origin of increased terrigenous supply to the NE South American continental margin during Heinrich Stadial 1 and the Younger Dryas, Earth Planet. Sc. Lett., 432, 493–500, https://doi.org/10.1016/j.epsl.2015.09.054, 2015.

Zhang, Y. C., Chiessi, C. M., Mulitza, S., Sawakuchi, A. O., Haggi, C., Zabel, M., Portilho-Ramos, R. C., Schefuss, E., Crivellari, S., and Wefer, G.: Different precipitation patterns across tropical South America during Heinrich and Dansgaard-Oeschger stadials, Quaternary Sci. Rev., 177, 1–9, https://doi.org/10.1016/j.quascirev.2017.10.012, 2017.